Production cycle optimization for pumping airborne wind energy systems

Tesi di Laurea Magistrale in
Automation and Control Engineering - Ingegneria
dell'Automazione

Author: **Rodolfo Mathis**

Student ID: 944621
Advisor: Prof. Lorenzo Mario Fagiano
Academic Year: 2021-22

Abstract

This thesis describes an approach to increase the efficiency of an Airborne Wind Energy (AWE) system with soft wing flying in crosswind motion. In AWE systems, power generation occurs in cycles, each consisting of a *Traction* phase where the cable is unwound and a phase called *Retraction* where the cable is rewound. Transition phases are required to go from the traction phase to the retraction phase (*Transition 1*) and vice versa (*Transition 2*).

The problem was first addressed, in the present work, through the efficiency of *Transition 1* and then through full-cycle optimization. Two ideas guided this work, one was to implement a control logic that guarantees a smooth transient behavior for the forces acting on the tether that ensure the maximum lifetime of the components. The other was to maximize the average cycle power production that is the key aspect of any energy production system.

Concerning the transition phase, two different control strategies that avoid abrupt increase in the force acting on the tether were implemented. The first one exploits the measure of the wind and ensures that the winch controller follows the desired reeling speed profile. The second implementation does not rely on wind measurements, which are often unreliable and not suitable for real world applications.

The optimal elevation-azimuth trajectory for the *Transition 1* at varying wind speed was computed based on a nonlinear optimization routine that aim to maximize the average cycle power of the kite. The solution found allowed also to obtain optimal values for the reel-in and reel-out velocities thus obtaining better overall cycle performances increasing the efficiency of the system. Therefore the initial goals have been achieved, providing new results compared to the state of the art, where the transition phase has not been well explored.

Keywords: Renewable Energy, Wind Energy, Airborne Wind Energy systems, Pumping Kite system, Transition phase optimization.

Abstract in lingua italiana

Questa tesi descrive un nuovo approccio per aumentare l'efficienza di un sistema AWE (Airborne Wind Energy) con ali flessibili che vola in configurazione crosswind. Nei sistemi AWE, la produzione di energia avviene in cicli, ognuno composto da una fase di trazione (*Traction*) dove il cavo viene srotolato ed una fase detta *Retraction* dove il cavo viene riavvolto. Per passare dalla fase di *Traction* a quella di *Retraction* e viceversa, sono necessarie fasi di transizione, rispettivamente *Transizione 1* e *Transizione 2*. Nel presente lavoro il problema è stato affrontato dapprima attraverso l'efficientamento della *Transizione 1* e poi attraverso l'ottimizzazione dell'intero ciclo. Due sono state le idee alla base di questo lavoro: una è stata quella di implementare una logica di controllo che garantisca un andamento regolare delle forze che agiscono sul cavo durante la *Transizione 1*, assicurando la massima durata dei componenti. L'altra è stata quella di massimizzare la produzione di energia per ciclo , aspetto chiave di qualsiasi sistema di produzione di energia. Per quanto riguarda la fase *Transizione 1*, sono state implementate due diverse strategie di controllo che evitano un brusco aumento della forza agente sul cavo. La prima sfrutta la misura del vento e assicura che il controllore del verricello segua il profilo di velocità di avvolgimento desiderato. La seconda implementazione non si basa sulla misura del vento, che spesso è inaffidabili e perciò non adatta alle applicazioni reali. La traiettoria in termini di elevazione ed azimut ottimale per la Transizione 1 al variare della velocità del vento è stata calcolata sulla base di una routine di ottimizzazione non lineare che mira a massimizzare la potenza media del ciclo del kite. La soluzione trovata ha permesso di ottenere anche valori ottimali per le velocità di arrotolamento e srotolamento, ottenendo così migliori prestazioni complessive del ciclo e aumentando l'efficienza del sistema. L'obiettivo iniziale è stato quindi raggiunto, fornendo nuovi risultati rispetto allo stato dell'arte, in cui la fase di transizione non è stata ben esplorata.

Parole chiave: Energia rinnovabile, Energia Eolica, Airborne Wind Energy systems, Pumping Kite system, Ottimizzazione delle transizioni.

Contents

1 | Introduction

1.1. Energy demand and sustainability

It is widely established that one of the biggest challenges of the 21st century is finding a solution to the problem of energy supply and production. Green energy, decarbonization, and circular economy are words that have become part of everyday language. Indeed, thanks to people's growing attention towards the problem of climate change, governments have been forced to take concrete actions in these directions.

The EU's energy policy states that: a variety of measures aiming to achieve an integrated energy market, security of energy supply and a sustainable energy sector, are at the core of the EU's energy policy [27]. Moreover one of the seventeen goals for a sustainable development that were adopted by all UN Member States in 2015, as part of the 2030 Agenda, is the goal of affordable and green energy [6].

Additionally, emerging markets and developing economies have a rapidly increasing energy demand and are consequently increasing energy production. Most scenarios predict that the global energy demand will increase between 10% and 20% over the next 10 years and up to 40% by 2050.

In order to get a better grasp on the current situation some quantitative data is needed. The scenario that the data reported in this chapter refers to is STEPS (Stated Policies Scenario). This scenario assumes an accelerated change in the power sector, which would be sufficient to realize a gradual reduction of emissions, assuming global electricity demand remained constant. However, the forecast predicts that global electricity demand will be growing steadily until at least 2050. Thus, in STEPS, almost all of the net growth in energy demand through 2050 is met by low-emission sources, but this leaves annual emissions around current levels. As a result, global average temperatures is expected to reach 2.6 °C above pre-industrial levels in 2100 [18].
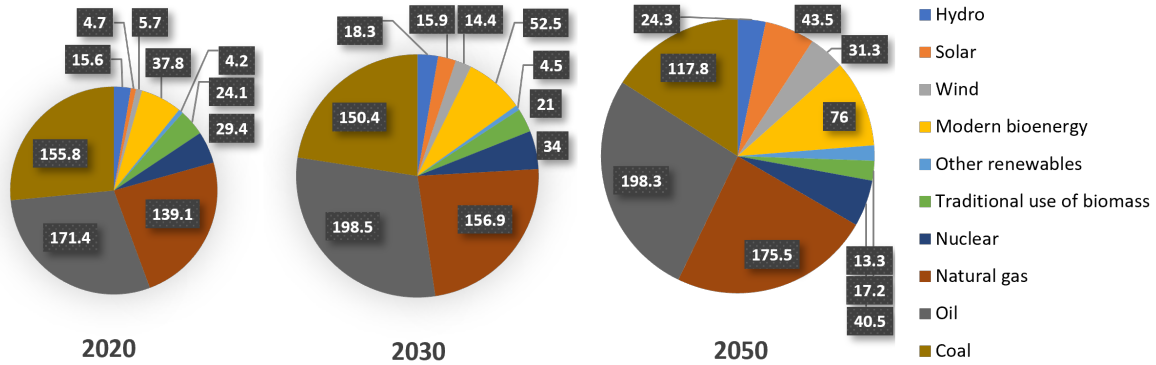
Figure 1.1: Comparison of current total energy demand (TES) to STEPS projected demand for the years 2030 and 2050, data is provided in EJ. The increasing area of the pie chart represents the growth in energy demand [18].

As it can be seen in figure 1.1, fossil sources currently account for about 79% of the total primary energy supply (TPES). The remaining 21% split between renewable energy (12%), biomass (4%) and nuclear energy (5%). In 2050, according to STEPS' projections renewable energy is expected to cover 26% of the grown total energy demand, with major increases expected from wind and solar powered technologies [18].

Recent events, such as the military invasion of Ukraine, have given a further boost to the energy transition especially in Europe. Indeed, renewable energy can be produced all over the globe while fossil sources are limited to a small number of countries, forming an oligopoly. Italian government, for example, has approved six new wind farms and has committed to further wind deployment [1]. On this scenario, finding competitive alternatives to the traditional fossil source, is a task that requires the joint effort of both academic research and companies.

1.2.   Wind energy and Airborne Wind Energy

Wind is generated by the movement of air masses from areas of high atmospheric pressure to areas of low pressure. Wind intensity and direction depend on a large number of factors on both local and planetary scales and has been a form of easily transformable local energy for millennia. Examples, such as mills or sailing boats testify how humans, already in past centuries, had understood its great importance. However, the fact that wind is found everywhere is not sufficient to make it a reliable energy source. Indeed, one of the key issues that must be solved to achieve independence from fossil fuels is overcoming the problem of intermittency of renewables. The demand for electricity must be met at all times and temporary interruptions are not allowed.

Typically the solution to this problem is to produce energy whenever wind is present and then store it if this is greater than the actual request. However, the storage of big amounts of electrical energy still have really high cost and thus alternative solutions that guarantee more reliable and constant production of energy are sought. A possible answer to this problem, concerning systems that harvest wind energy, is to go higher. At an altitude of $500 - 1000$ meters, wind is much more constant and also has a higher speed than on the ground level. Reaching this altitude is impossible for wind turbines but might be reachable for airborne wind energy technology in the next years, as better explained below. Besides, increasing the number of sites for traditional wind farms will not be enough to supply for the future increasing energy demand and deep offshore wind farms are very expensive. Thus, it makes sense to look for other technologies to further increase the production capacity. Of all the renewables, wind and sun power technologies are the ones undergoing the fastest growth (see figure 1.1), even if nowadays hydro-power is the most relevant and cost-efficient technology, accounting for 3% of TES and about 16% of global electricity generation. Due to the fact that most of the suitable sites are already exploited, hydro-power has little chance to grow further. In contrast, wind and sun have a much grater potential.

1.2.1. Wind turbines

Wind turbines represent the natural evolution of the old mils and are thus, an established technology spread around the globe. In order to increase the production and to be able to reach the wind at greater heights, the size of the turbines is continuously growing (see figure 1.2).

The structure dimensions and the necessary safety distance that has to be kept from houses, have forced wind farms to be build far from the city and is one of the reason why most of the current research is oriented towards building off-shore wind farms. Building a solid foundation for off-shore wind turbines of this size is still an open topic and highlights the weakness of this technology: the high costs and investment required to build a new wind farm, and also their impact on the landscape and the fauna surrounding them. In figure 1.3 it can be seen how the costs of a single on-shore turbine is distributed on its components. It is immediately clear that more then a quarter of the entire cost is due to the tower and this percentage further increases for off-shore wind turbines.
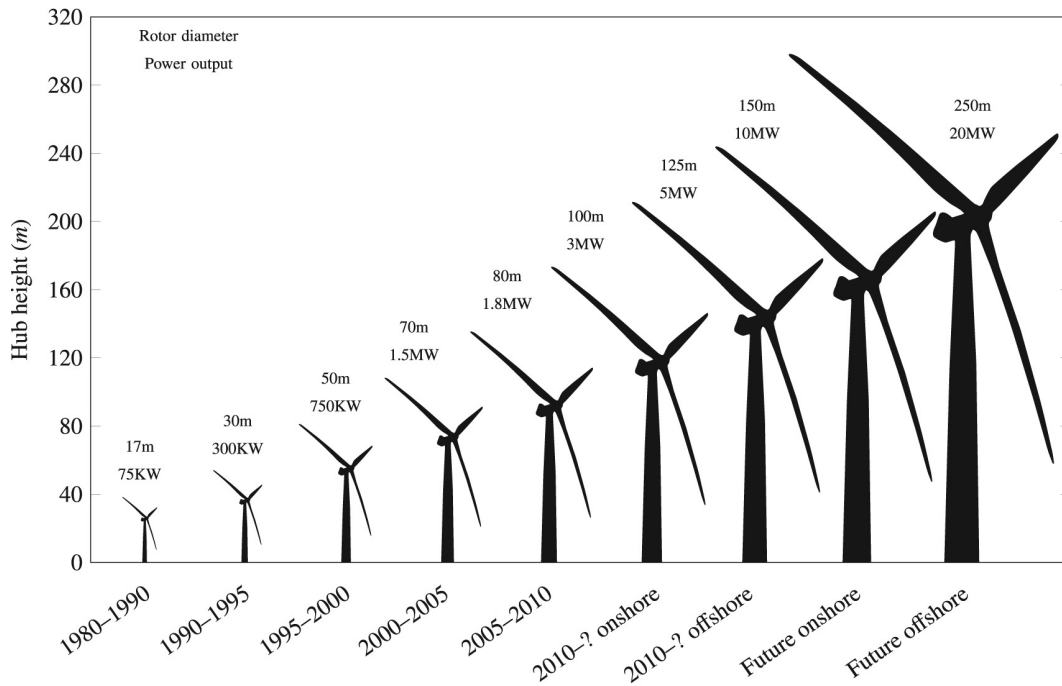
Figure 1.2: Development of wind turbine size [8].

Bottom line, despite their success, wind turbines are severely limited by their support structure, which makes them very expensive and also precludes the possibility of exploiting high-altitude wind. This is the reason that led to the development of a new concept of wind energy systems, the so-called airborne energy systems, capable of potentially harnessing wind at high altitudes.

Figure 1.3: Cost of the components of a wind turbine as a fraction of the total cost in percent [7].

1.2.2. Airborne Wind Energy

The basic principle of Airborne Wind Energy (AWE) dates back to the 1980s by Loyd [26]. His paper analyzed, from a purely theoretical point of view, the max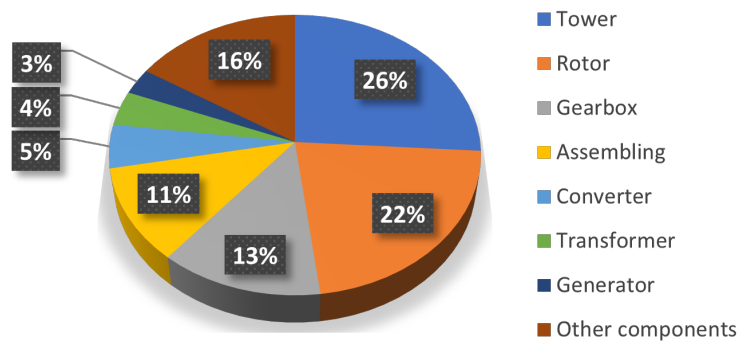imum energy that can be extracted with AWEs based on tethered wings. However, due to the technical difficulty, this technology had to wait a few more decades before the first prototypes could be built. Nowadays, a few commercial models are available, but AWEs full potential is still to be determined.

Since AWE is a technology that is still in its infancy and it is aiming for deployment in a variety of markets and applications, many technology approaches, concepts of operation, and designs are under consideration. A first main differentiation is related to the energy generation. The energy can be produced on board of the flying devices (fly-gen AWE) or at the ground station (ground-gen AWE). A second subdivision characterizes the groups with respect to the type of flight operation:

Crosswind A flight path designed to increase relative speed of the kite and maximize swept collection area. The flight path can be implemented through figure eights patterns or circles patterns.

Tether-aligned A flight path that aligns with the direction of the tether, potentially reducing both the importance of tether drag and the opportunity to sweep the area.

Rotational A rotor-type system with a circular flight path of rotational units lifted at operational altitude (e.g. see [28]).
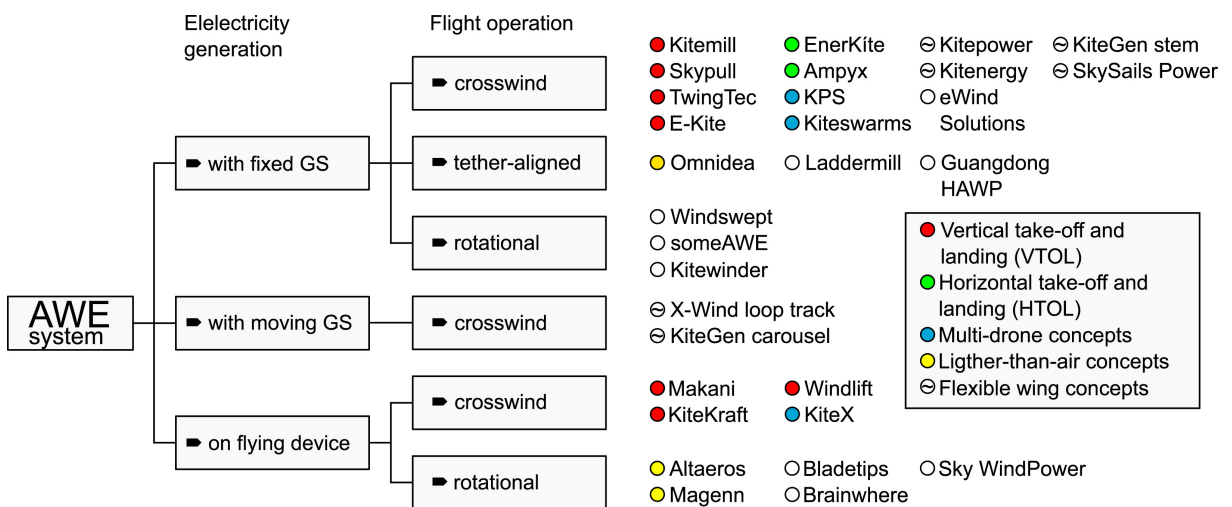

Figure 1.4: Classification of traditional AWE technology archetypes [29].

Other characterization methods are related to the building design of the flying structure. There are flexible wing (such as kite sails) and rigid wing devices but also multi-drone concepts and many other approaches. Also, the take-off and landing procedure can be used to distinguish between different models. These maneuvers are strictly related to the structural design choices. A more detailed explanation can be found in [23], [30], [13] .

For each of these different solution there are ongoing research projects, as can be seen in figure 1.4. As of today it is not clear which which of these implementations will be more successful. However, the recent commercialization of the first SkySails Power SKS PN-14 systems [4] suggest that this might be one of the solution that best fit the state of the technology.

In this work the AWE system that will be analysed is similar to the one sold by SkySails and shown in figure 1.5. It consists of a fixed ground station generating the energy and a flexible wing flying an eight figure path in crosswind.

Figure 1.5: Skysails Power SKS PN-14 system. Courtesy of the SkySails Group

1.3.   Basic operating principles of a pumping AWE system using a soft kite

In the previous paragraph different designs for AWE systems were introduced, while here the basic operating principle of a soft kite is briefly explained (see section 3.1 for more details).

From a functional point of view, the system is composed of three macro elements: the kite, the ground station where the generator is located and the cable that connects the two elements. The sail flies as it is blown by the wind and applies tension on the tether. The unreeling of the tether from the drum produces a rotational motion that is transformed into electrical energy using a generator. The duty cycle is composed of four phases:

TRACTION: During this phase the energy is produced, the tether is reeled out while high forces are acting on the sail.

TRANSITION 1: This phase manages the kite's transition from the end of the *Traction* to the beginning of the *Retraction*.

RETRACTION: Energy is used to retract the cable to enable the start of a new cycle. This operation is done while the kite is positioned out of the wind such that less energy is used to reel-in than what was produced during the *Traction*.

TRANSITION 2: After the tether is completely reeled in, this phase ensure that the kite position is the one desired to be able to start the next productive cycle.
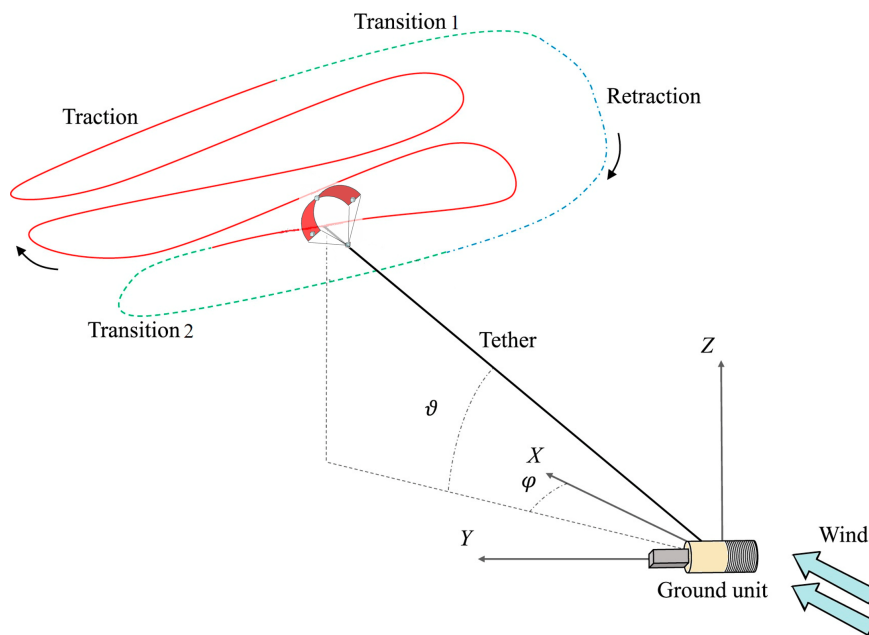

Figure 1.6: The production cycle of the system, giving emphasis to each one of the phases. Adapted from [20]

In order to get the kite on air running, it has to take off from the ground. However, this maneuver and the landing procedure are not considered this work,which focuses on the generation cycle.

1.4.   Innovative aspects of the thesis

Economic feasibility is crucial for any commercial solution, and that is where the efficiency of the energy harvesting plays a key role. This thesis aims to contribute to this goal by studying and analysing one of the four phases of the kite's production cycle, the so called *Transition 1* (shortly $T1$).

Not much can be found in the literature about the optimal solution to fly the kite from the end of the production phase to the beginning of the *Retraction* phase. At the transition's starting point the tether has been reeled-out almost completely and the forces exerted on the sail and on the tether, are really high. It means that it is likely that the switching instant is a sensible point regarding the safety of the system. A wrong switching behaviour between the controller of the *Traction* phase and the controller of the transition can generate sudden force peaks that, in the worst case, could lead to the tether or sail braking. So the problem treated in this work is crucial not only for the average power production, but also with regard to the maintenance and the component's lifetime, especially for the tether.

Different attempt were made in order to find an optimal solution for the implementation of the *Transition 1*, maximising the average power production which is the key aspect of any energy production system. The final solution exploits the system model structure that allows the design of the trajectory controller decoupled from the winch controller. The guidance system implemented for the *Transition 1* is based on few target points (see section 2.5), while for the other controller two difference strategies were designed in order to reach the desired behavior. One exploits the physical knowledge of the system but has the drawback that it needs an estimate of the nominal wind speed. The second solution achieve similar result by imposing a desired saturation on the control actuator. Briefly, the key contribution of the thesis can be summarized as:

- Implementation of two different control structures for the winch controller during *Transition 1* that avoid force peaks on the tether. One independent from the nominal wind measurement and one that exploits this data.

- Formulation and solution of a nonlinear optimization program to compute the best trajectory for the *Transition 1* that maximise the average cycle power as the wind speed varies.

1.5.   Thesis outline

The work in this thesis is structured as follows:

Chapter 2 - System model : here the model of the system is presented. The description starts with the presentation of the point mass model of the sail, the model of the tether and the one of the ground station. Then the focus moves to the control structure.

Chapter 3 - Optimal Cycle Parameters illustrates, at first, the different cycle's phases for an AWE system, it highlights which are the key parameter for each one of the phases. Then the innovative control logic for the *Transition 1* is presented along with the trajectory optimization problem.

Chapter 4 - Simulation Results deals with the results of the control logic implemented on the *Transition 1* and presents the results of the trajectory optimization.

Chapter 5 - Conclusion describes the conclusion of the thesis and some future works to be done.

2 | System model

As stated in the previous chapter the study is based on a pumping AWE system that consists of the kite's sail, and a tether (or two tethers, depending on the Kite model) that links it to the ground station. At the ground station, the cable is operated by a winch that is connected to a power generator through a gearbox to produce power.

As just mentioned kite systems can be differentiated by the presence of one or two tether which influences the flight maneuvering actuation system.

- two tethers configuration: the maneuvering (steering) actuation system is located on the ground station.

- one tether configuration: the maneuvering (steering) actuation system have to be placed on a unit at the end of the tether (SU: steering unit); from the SU two pairs of cables exit and connect to the two sides of the wing.
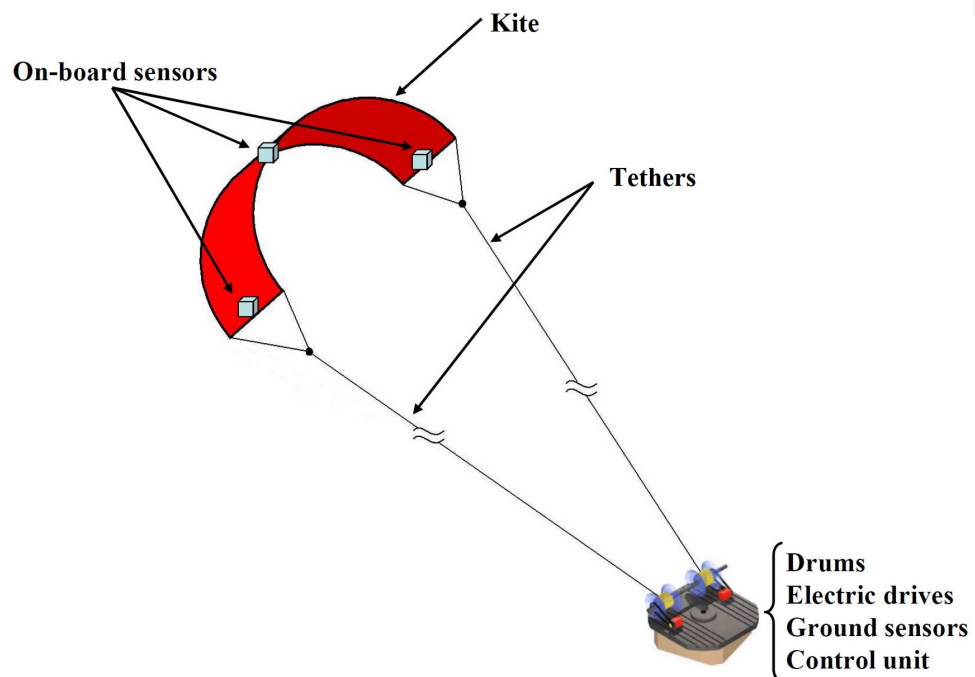

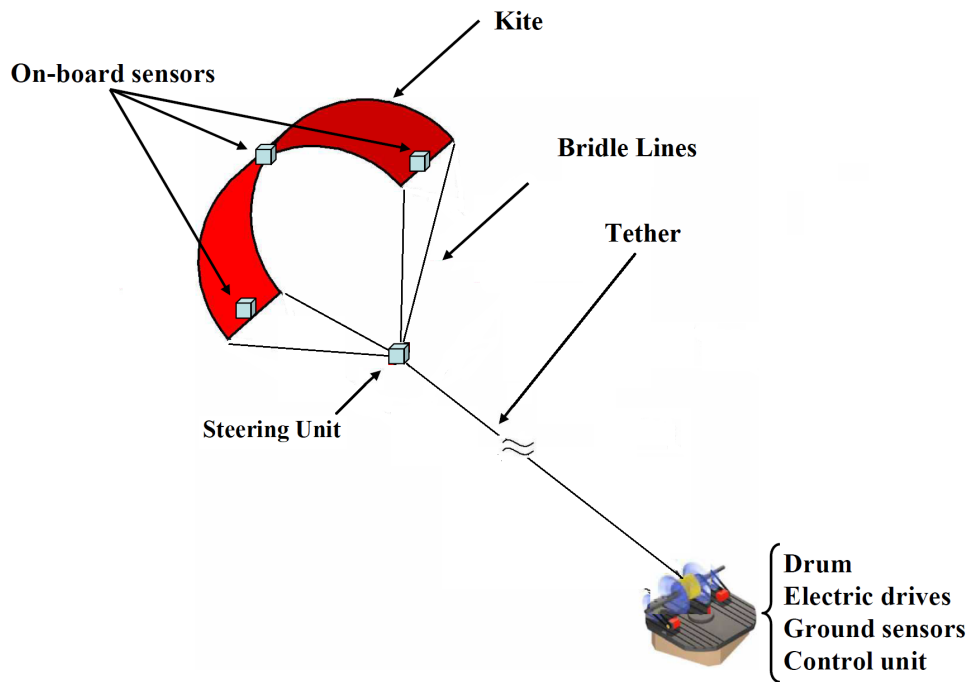Figure 2.1: Two tethers Kite configuration [24].

Figure 2.2: One tether Kite configuration. Adapted from [24].

In either configuration, on-board sensors are attached on the kite's wing (see figure 2.1 and 2.2)

2.1.   Kite model

A dynamic model of the described system can be derived from first principles where the wing is assumed to be a point with given mass. The adopted model has been developed in [24] and here briefly resumed. For the modellization two main reference systems are considered: a fixed, inertial frame G (X,Y,Z), centered at the ground unit (GU) and a local frame L $(e_\theta, e_\varphi, e_r)$ centered on the center mass of the kite (see figure 2.3). The X axis is assumed to be parallel to the ground and aligned with the longitudinal symmetry axis of the GU, the Z axis is perpendicular to the ground pointing upwards, and the X axis is such that it forms a right hand system.
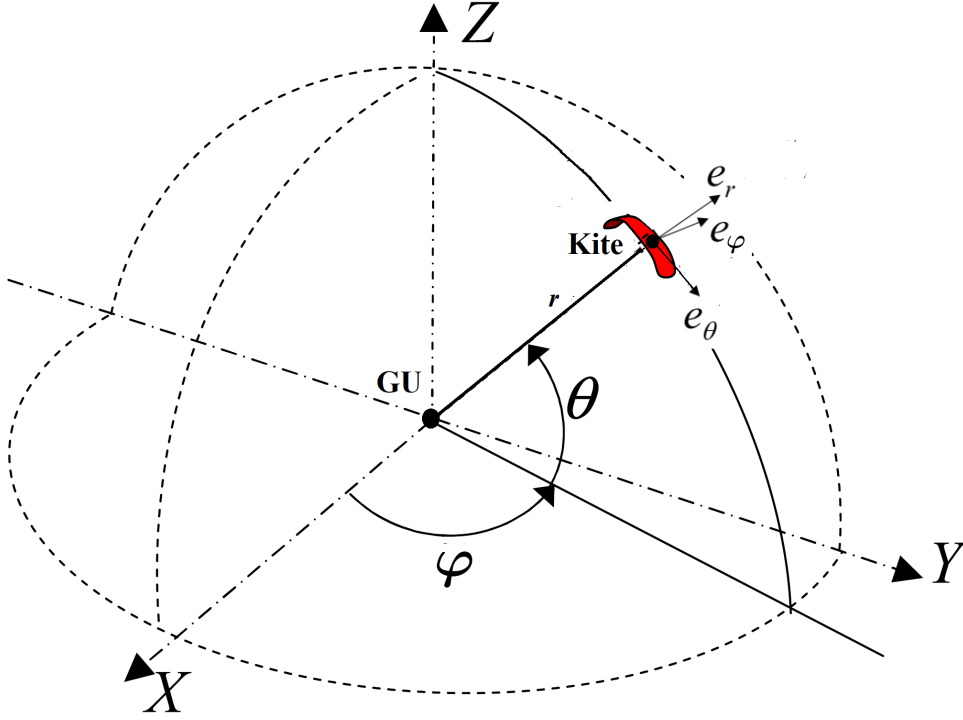
Figure 2.3: Reference Systems. Adapted from [24]

The origin of the local frame, i.e the kite (point mass) position, can be expressed in spherical coordinates as a function of its distance from the origin and of the two angles θ and φ , as depicted in figure 2.3, which also shows the three unit vectors $(e_\theta, e_\varphi, e_r)$ of the local coordinate system. Unit vectors can be expressed in the local system by the following rotation matrix :

$$R = \begin{bmatrix} sin(\theta)cos(\varphi) & -sin(\varphi) & cos(\theta)cos(\varphi) \\ sin(\theta)sin(\varphi) & cos(\varphi) & cos(\theta)sin(\varphi) \\ -cos(\theta) & 0 & sin(\theta) \end{bmatrix} \tag{2.1}$$

The matrix R defined is a rotational matrix, this means that it is an ortogonal matrix with norm equal to one. The ortogonality condition allows to compute easily also the inverse of this transformation, since the inverse of is just the transposition of the original matrix i.e. $(R^{-1} = R^T)$.

For simplicity, it has been assumed that the nominal wind direction is aligned with the X axis of the GU, denoted by X axis. This assumption is not limiting since this condition can be achieved by properly orienting the GU, exploiting a measure, or estimate of the nominal wind direction. In addition, as stated in [22] from experimental results, it was

verified that misalignment of the GU with respect to the wind direction up to $\pm$ 30°
up did not affected significantly the kite path. The dynamic model of the kite's motion
can derived applying Newton's laws and in the local coordinate system L $(e_\theta, e_\varphi, e_r)$ the
following equations are obtained:

$$\ddot{\theta} = \frac{F_\theta}{mr}$$
$$\ddot{\varphi} = \frac{F_\theta}{mr \sin(\theta)} \tag{2.2}$$
$$\ddot{r} = \frac{F_r}{m}$$

where m is the kite mass and F_θ, F_φ and F_r are the three force components along the
local axis. These forces include the contribution of gravity force F_{grav} (of the kite and the
tether), the apparent force F_{app}, the aerodynamic force F_{aer} and traction force F_{tr} due to
the interaction with the tether as reported in the following equation.

$$F_\theta = F_\theta^{grav} + F_\theta^{app} + F_\theta^{aer} + F_\theta^{aer,c}$$
$$F_\varphi = F_\varphi^{grav} + F_\varphi^{app} + F_\varphi^{aer} + F_\varphi^{aer,c} \tag{2.3}$$
$$F_r = F_r^{grav} + F_r^{app} + F_r^{aer} + F_r^{aer,c} - F_r^{tr}$$

In the following subsections the single terms will be briefly detailed (further details can
be found in [24].

2.1.1.   Gravitational force

To compute the magnitude of the F_{grav} component applied to the kite center of gravity,
the contribution of both the kite and the tether have to be considered. Assuming that
the mass of tether is concentrated at weight at half its length (i.e. r=2), the magnitude
of the equivalent weight force F_{grav_tether} applied at the kite center of gravity is the (for
further details see [24], here adapted to the presence of just one tether):

$$|\vec{F}_{grav\_tether}| = \left(\frac{\pi \rho_t d^2 r}{8}\right) g \tag{2.4}$$

where ρ_t is the material density, d is the tether diameter and r is the distance from the
origin (thus the tether length).

The overall gravity force magnitude is:

$$|\vec{F}_{grav}| = \left(m + \frac{\pi \rho_t d^2 r}{8}\right) g \tag{2.5}$$

where m is the kite mass.

The gravity force as expressed in ((2.5)) is considered applied at the kite point mass and directed downward with respect to the Z-axis of the fixed frame G(X,Y,Z). Using the rotation matrix (2.1) To express it in the local frame L $(e_\theta, e_\varphi, e_r)$, we get:

$$\vec{F}_{grav} = \begin{bmatrix} F_\theta^{grav} \\ F_\varphi^{grav} \\ F_r^{grav} \end{bmatrix} = \begin{bmatrix} \left(m + \frac{\pi \rho_t d^2 r}{8}\right) g\cos(\theta) \\ 0 \\ -\left(m + \frac{\pi \rho_t d^2 r}{8}\right) g\sin(\theta) \end{bmatrix} \tag{2.6}$$

2.1.2. Apparent forces

During kite motion additional forces act on the kite; in particular, for the AWE which is characterized by the KG–yoyo configuration flight (see [24]) the following apparent forces have to be considered:

$$\vec{F}_{app} = \begin{bmatrix} F_\theta^{app} \\ F_\varphi^{app} \\ F_r^{app} \end{bmatrix} = \begin{bmatrix} m\left(\dot{\varphi}^2 r \sin(\theta)\cos(\theta) + 2\dot{r}\dot{\theta}\right) \\ m(-2\dot{r}\dot{\varphi}\cos(\theta) + 2\dot{\varphi}\dot{\theta}r\sin(\theta)) \\ m\left(r\dot{\theta}^2 + r\dot{\varphi}^2 \cos(\theta)^2\right) \end{bmatrix} \tag{2.7}$$

2.1.3. Aerodynamic forces

As known from fluid dynamics, the kite while moving with respect to the surrounding fluid, the air, is subject to drag and lift forces which depend on the effective wind speed $\vec{W}_e$. This in the local system L $(e_\theta, e_\varphi, e_r)$ can be expressed as:

$$\vec{W}_a = \vec{W} - \vec{W}_{kite} \tag{2.8}$$

where $\vec{W}$ is the wind speed and $\vec{W}_{kite}$ is the kite speed with respect to the ground. In the local system L $(e_\theta, e_\varphi, e_r)$ $\vec{W}_{kite}$ takes the form:

$$\vec{W}_{kite} = \begin{bmatrix} -\dot{\theta}r \\ \dot{\varphi}r\cos(\theta) \\ \dot{r} \end{bmatrix} \tag{2.9}$$
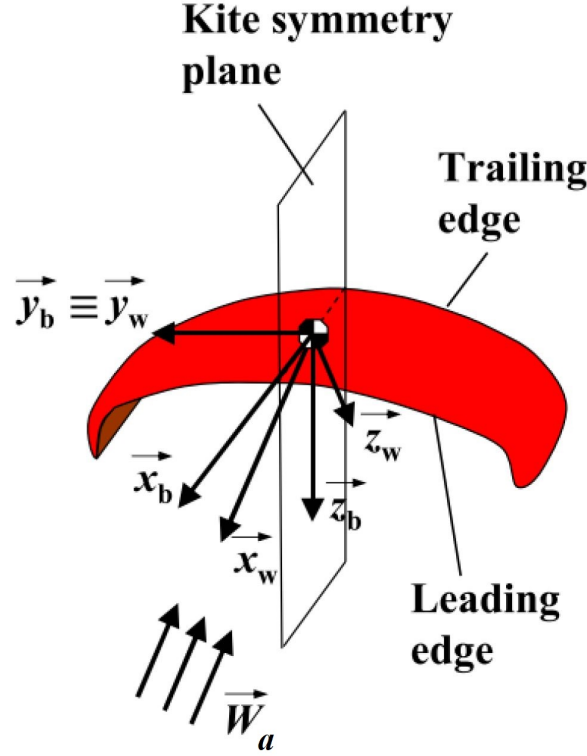
Figure 2.4: Wind Reference System [24].

To compute the aerodynamic force, a wind coordinate system, $L_w(x_W, y_W, z_W)$ is defined which is centered in the kite center of gravity. As shown in figure unit vector x_w is aligned with the apparent wind speed vector and directed from the trailing edge of the kite's wing to its leading edge, unit vector z_w is contained in the kite symmetry plane and is pointing downwards from the top of the kite; finally unit vector y_w is defined so to complete a right hand system.
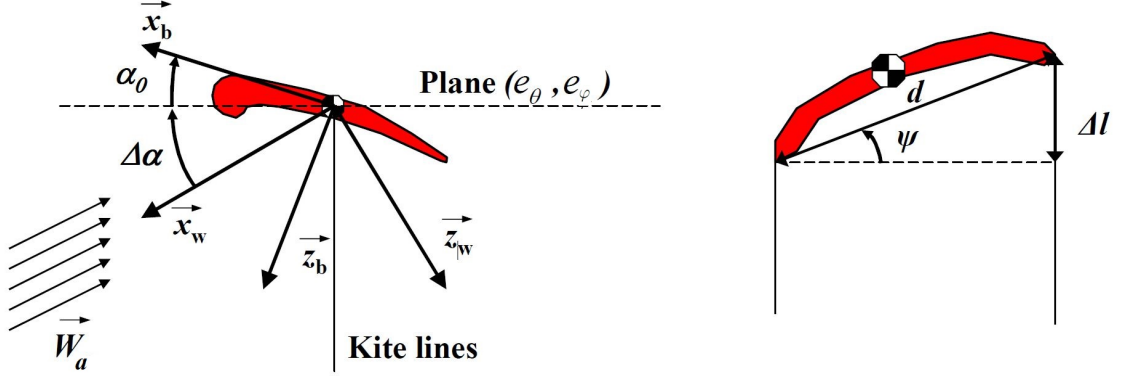
x_W can be written in the local coordinate frame L $(e_\theta, e_\varphi, e_r)$ as:

$$\vec{x}_W = -\frac{\vec{W}_a}{|\vec{W}_a|} \tag{2.10}$$

The expression of y_W in the local coordinate system is equal to (see [24] and references herein)

$$\vec{y}_W = e_W(-\cos(\psi)\sin(\eta)) + (e_r \times e_w(\cos(\psi)\sin(\eta)) + e_r\sin(\psi) \tag{2.11}$$

where:

Figure 2.5: $\Delta\alpha$, α_0 and ψ angles definition [24].

$$
e_W = \frac{\vec{W}_a - e_r \left(e_r \vec{W}_a \right)}{\left| \vec{W}_a - e_r \left(e_r \vec{W}_a \right) \right|}
$$

$$
\eta = \arcsin \left(\frac{\vec{W}_a e_r}{\vec{W}_a - e_r \left(e_r \vec{W}_a \right)} \tan(\psi) \right)
$$

(2.12)

ψ variable in 2.12 is an important variable: it is the control input of the system (as shown in section 2.5). It is defined as:

$$
\psi = \arcsin \left(\frac{\Delta L}{d} \right)
$$

(2.13)

where, as shown in figure 2.5, d is the wingspan and ΔL is the length difference of the two bridle pair lines (see figure 2.2). ΔL is considered positive if, looking the kite from behind, the right line is longer than the left one.

Finally, the wind unit vector y_w is computed as

$$
\vec{z}_W = \vec{x}_W \times \vec{y}_W
$$

(2.14)

to complete the tern.

Given the above definitions and equations, the aerodynamics force $\vec{F}^{aer}$ in the local frame L $(e_\theta, e_\varphi, e_r)$ are given by:

$$
\vec{F}^{aer} = \begin{bmatrix} F_\theta^{aer} \\ F_\phi^{aer} \\ F_r^{aer} \end{bmatrix} = -\frac{1}{2} C_D A \rho \left| \vec{W}_a \right|^2 \vec{x}_W - \frac{1}{2} C_L A \rho \left| \vec{W}_a \right|^2 \vec{z}_W
$$

(2.15)

where ρ is the air density, A is the kite characteristic area, C_L and C_D are the lift and the drag coefficients. The C_L and C_D coefficients are not constant but they depend on the wing's angle of attack α, which in turn varies in times as function of the kite flight state. To define the angle α an additional body coordinate system $L_b(x_b, y_b, z_b)$ needs to be introduced (see figures 2.4, 2.5), centered in the kite center of gravity. The angle α is defined as the angle between the wind axis $\vec{x}_w$ and the body axis $\vec{x}_b$. For details on $L_b(x_b, y_b, z_b)$ see, for example, [24] and [12].

Tether Contributions

In addition to the weight force (see 2.1.1) the tether influence the kite motion exerting aerodynamic and traction forces. The aerodynamic force contribution $\vec{F}^{t,aer}$ is due to the drag and, in local coordinates $(e_\theta, e_\varphi, e_r)$, a conservative estimate of the line drag force is equal to [24]:

$$\vec{F}^{\mathrm{t,aer}} = \begin{bmatrix} F_\theta^{\mathrm{t,aer}} \\ F_\varphi^{\mathrm{t,aer}} \\ F_r^{\mathrm{t,aer}} \end{bmatrix} = -\frac{\rho C_{D,l} A_l \cos(\Delta\alpha)}{8} \left| \vec{W}_a \right|^2 \vec{x}_{\mathrm{w}} \tag{2.16}$$

where ρ is the air density, $C_{D,t}$ is the drag coefficient of the tether, A_t is the cross-sectional area of the tether, $\vec{W}_a$ is the apparent wind speed. The variable $\Delta\alpha$ is the angle between the apparent wind vector $\vec{W}_a$ and the tangent plane to the wind window at the wing's location. The traction force contribution $\vec{F}^{t,trc}$ of the tether is always directed along the local unit vector e_r and cannot be negative, since the kite can only pull the lines.

In the following section, a more accurate tether model is presented and the tether contributions (2.4) and (2.16) will be recomputed.

2.2. Tether model

In literature many different approaches to model the kite's tether have been proposed. Most often the tether is simply modelled as a "straight line": the tether is considered as an ideal beam (inextensible and rigid). The tether force contributions described in the previous sections refers to this assumption. In [31] the tether is modeled as a collection of lumped masses connected by inelastic links and to derive the equations of motion in generalised coordinates a Lagrangian approach has been adopted. Point masses are added and removed to account for the reel-out and reel-in of the tether. In [25] the kite and the tether are modeled as a particle system, using discrete point masses which are connected

by spring-damper elements.

In [17] the cable is discretized into an assembly of N linear elements. The mass of the cable is lumped at the N +1 node points. To model the elasticity of the true cable, each visco-elastic cable element is idealized as a parallel combination of an ideal spring and a viscous damper.

In this work, the tether model developed in [9] [15] is adopted. This consist of multi-body modellization of the tether, derived as an extension of the one described in [10]. The tether is discretized in segments and its mass is split into a N point mass nodes; each segments is modelled as a spring-damper system. By adding the points at the extremes, assumed to be fixed to the kite and to the ground station, the resulting number of segment is N + 1 segments; each inner node is subject to its own weight, to the aerodynamic force, and to the forces applied by the two neighboring tether segment.

In the following each single contribution will be computed. The mass of each inner node m_{node} is computed taking into account the mass of the whole tether M and the number of nodes N:

$$m_{node} = \frac{M}{N} = \frac{\rho_t \pi d^2 r}{N} \tag{2.17}$$

where ρ_t is the material density, d is the tether diameter and r is the tether length. The masses of the two extreme nodes are the mass of the ground station and the kite, respectively.
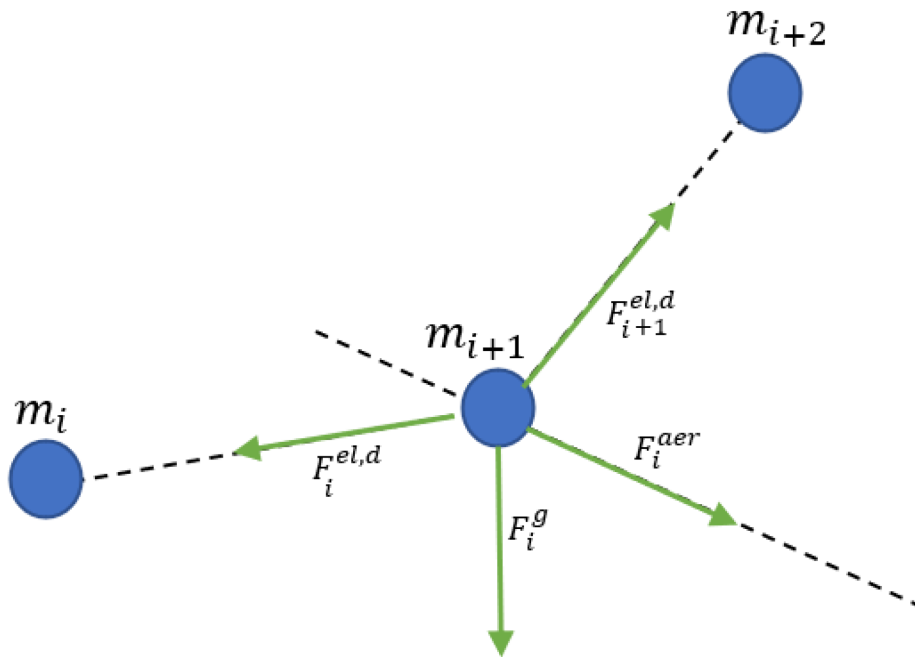

Figure 2.6: Force contribution on $i - th$ node of the tether [15].

2.2.1. Tether gravitational force

The gravitational force that acts on each internal nodes is directed in the direction of the z-axis pointing downward as depicted in figure 2.6. Its magnitude, for each of the N nodes, is given by:

$$|F_i^g| = m_{node}g \quad \text{for} \quad i = 1 \dots N \tag{2.18}$$

2.2.2. Tether elastic and damping force

The tether is equally divided so the nominal length of each segment, given the actual total length r of the tether when no elongation is jet exerted, is

$$l_{node} = \frac{r}{N} \tag{2.19}$$

On the tether, due to its physical structure, the tension force arises only if there is an elongation with respect to the nominal length, while,on the contrary, it is assumed that no compression with respect to the nominal length can be exerted. On each tether segment the tension force acts merely along the segment direction (see figure 2.6), which is computed for the $i - th$ segment from the position of the pair nodes $(i, i+1)$.

Denoting $\vec{p_i}$ the coordinates position vector of a node, the actual segment vector $\vec{s_i}$ is computed as:

$$\vec{s_i} = \vec{p}_{i+1} - \vec{p_i} \tag{2.20}$$

The applied non linear elastic force magnitude for each of the N+1 segment can be computed as:

$$F_i^{el} = k_{node} \max(0, |s_i| - l_{node}) \frac{\vec{s_i}}{|s_i|} \tag{2.21}$$

where $|\vec{s_i}|$ represents the actual length of the element and l_{node} its corresponding nominal length, while k_{node} is the spring constant of the single element. In (2.21) the saturation to zero implies that no elastic force is present for compression, i.e. when the distance between two nodes is smaller than the nominal segment length. The spring constant k_{node} for each element is computed approximating the segments' chain as a series of springs (and dumpers), and is given by:

$$k_{node} = K(N + 1) \tag{2.22}$$

where K is the spring constant of the entire tether.

Each segment of the tether has been modeled as a spring-damper system. On each segment, the damping effects of the tether are supposed to act only along the segment direction and are computed as:

$$\vec{F}_i^{damp} = c_n \frac{\vec{v}_i^T . \vec{s}_i}{|s_i|^2} \vec{s}_i \tag{2.23}$$

where, c_n is the damp constant of each element and is computed as [15].

$$c_n = C(N+1) \tag{2.24}$$

and given the velocity vector of the point mass node i-th $\vec{p}_i$, $\vec{v}_i$ is computed as

$$\vec{v}_i = \vec{p}_{i+1} - \vec{p}_i \tag{2.25}$$

2.2.3.   Tether aerodynamic force

As for the kite, each segment of the tether is also subjected to aerodynamic forces. In practice, the lift component can be neglected, due to its low lift coefficient and the drag aerodynamic effect is computed as [9],[25].

$$F_i^{aer_d} = \frac{1}{2} C_{d,t} A_{t,i}^{\perp} \rho_a \left| \vec{v}_i^a \right| \vec{v}_i^a \quad \text{for} \quad i = 1 \ldots (N+1) \tag{2.26}$$

where $C_{d,t}$ is the drag coefficient of the tether, ρ_a is the air density, and $A_{t,i}^{\perp}$ is the projection of the surface of tether segment i-th on a plane perpendicular to the apparent wind velocity $\vec{v}_i^a$ at the i-th node; knowing $\vec{v}_i^w$, i.e.the velocity vector of the wind at the node, the latter is computed as:

$$\vec{v}_i^a = \vec{v}_i^w - \vec{v}_i \tag{2.27}$$

Finally, having computed all the force components acting on the tether, the total force on each internal node can be written as [15]:

$$\vec{F}_i^{tot} = \vec{F}_i^g + \vec{F}_{i+1}^{el} - \vec{F}_i^{el} + \vec{F}_{i+1}^{damp} - \vec{F}_i^{damp} + \frac{1}{2}(\vec{F}_{i+1}^{aer}{}^{-d} + \vec{F}_i^{aer_d}) \quad i = 1 \ldots N \tag{2.28}$$

The last term in (2.28) account for an average of the aerodynamic forces acting on the two adjacent tether segments.

As stated in the previous, taking into account that the tether is linked to the ground station and to the kite, two nodes have been added to the N internal nodes. The total force due to the tether here have be computed as [15], [9]:

$$\vec{F}_0^{tot_t} = \vec{F}_1^{el} + \vec{F}_1^{damp} + \frac{1}{2}\vec{F}_1^{aer\_d}$$
$$\vec{F}_{N+1}^{tot_t} = -\vec{F}_N^{el} - \vec{F}_N^{damp} + \frac{1}{2}\vec{F}_N^{aer\_d}$$

(2.29)

where node 0 is the ground station and node N+1 accounts for the kite.

These equations have to be taken into account when coupling the tether model with the two connected systems, the winch, at the ground end and the kite at the other end, substituting, as previously stated equations (2.4) and (2.16).

Note that to obtain the total force at the kite point mass in local coordinate, the tether contribution has to be moltiplied by the rotational matrix R defined by equation (2.1).

2.3. Ground station

The ground station handles the tether and converts mechanical power to electrical power. It consists of a winch drum, a gearbox, an electric drives able to act either as generators or as motors and a converter all withing a steel structure with foundation. In addition, power electronics for grid connection and/or battery storage system are key components.

Figure 2.7 refers to the Skysails Power SKS PN-14 system and details the power kite system components. It can be noted the presence of the mast that is used during the launch and landing phases. These phases are not considered in the present work. Ground station are typically equipped with the sensors to measure tether length, angle, and speed as well as ground wind speed and direction.

The design and construction specifications of the two main components, the drum and the electric machine, will be briefly described below.

2.3.1. Drum winch

The drum is made by a hollow steel cylinder (density equal to $\rho_{steel} = 8000 \text{ kg m}^{-3}$) closed at the ends by two steel disks (see 2.8).

In 2.1 drum typical geometric parameters are specified. For AWE systems the drum are generally custom made for each single system application since its length has to be adapted to the system configuration, i.e mainly its cable length.

Figure 2.7: Example of Kite system (Skysails Power SKS PN-14 system):1 ram-air kite, 2 steering unit, 3 main tether, 4 launch and landing mast, 5 ground station housing, 6 winch with generator and gearbox, and 7 concrete foundation plate. Courtesy of the SkySails Group [23]
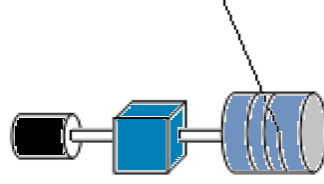
Considering the thickness d_{tether} (diameter) of the tether and its maximum length L_{max}, and assuming no overlap of the tether between each winding and when is completely reel in (worst case scenario), the required drum length can be computed as:

$$L_{cy} = \left(\frac{L_{max}}{2\pi r_{2cy}} \right) \quad d_{tether} \tag{2.30}$$

where r_{2cy} is the cylinder outer radius.
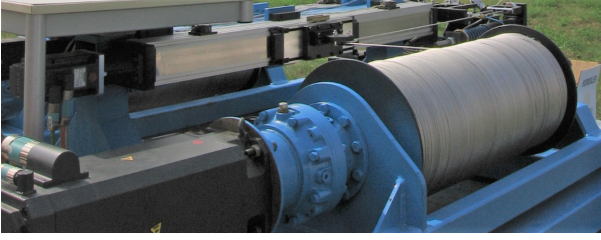
(a)   (b)

Figure 2.8: An example of winch drum with gearbox and electric motors (a) and its schematic representation (b). Adapted from [24]

The winch is modelled by a rather standard, linear time invariant rotational mechanical system. Using parameters in table 2.1 the mass of the cylinder and the disk are computed by:

$$
\begin{aligned}
m_{\text{cylinder}} &= \pi \rho_{\text{steel}} \, L_{cy} \left(r_{2cy}^2 - r_{1cy}^2 \right) \\
m_{\text{disk}} &= \pi \rho_{\text{steel}} \, r_d^2 s_d
\end{aligned}
\tag{2.31}
$$

and from the definition of momentum of inertia we have:

$$
\begin{aligned}
J_{\text{cylinder}} &= \frac{1}{2} m_{\text{cylinder}} \left(r_{2cy}^2 + r_{1cy}^2 \right) \\
J_{\text{disk}} &= \frac{1}{2} m_{\text{disk}} \, r_d^2
\end{aligned}
\tag{2.32}
$$

Finally, the total inertia moment of the drum is

$$
J_{\text{tot}} = J_{\text{cylinder}} + J_{\text{disk}}
\tag{2.33}
$$

2.3.2. Electric machine

The winch drum is connected to the electric machine by a gearbox as schematically represented in (2.8b).

Table 2.1: Cylinder and Disks constructive parameters

Drum Cylinder		
Outer radius	r_{2cy}	0.5 [m]
Inner radius	r_{1cy}	0.48 [m]
Thickness	s_{cy}	2 [mm]

Drum Disk		
Radius	r_d	0.5 [m]
Thickness	s_d	5 [mm]

The dynamical equations of the overall momentum from the motor side and the drum (load) side are, respectively:

$$J_m \dot{\omega}_m = T_m - T_{tm} - c_{f_m} \omega_m - \tau_{s_m} \operatorname{sign}(\omega_m)$$
$$J_l \dot{\omega}_l = T_{tl} + T_l - c_{f_l} \omega_l - \tau_{s_l} \operatorname{sign}(\omega_l)$$

(2.34)

In (2.34) the quantities characterized by the subscript m denote engine parameters, while the one characterized by l denote the drum parameters. T_m is the torque generated from the motor and T_l is the one transmitted to the final load, i.e the drum, ω_m and ω_l are the angular speeds, c_{f_m}, τ_{s_m} and c_{f_l} ,tau_{s_m} are the viscous and static friction coefficients, respectively.

Denoting by n the gear ratio of the drivetrain and recalling that is the ratio of the angular speed of the input gear to the angular speed of the output gear and that the input and output torque are inversely related we can write:

$$n = \frac{\omega_m}{\omega_l}$$
$$n = \frac{T_{tl}}{T_{ml}}$$

(2.35)

Substituting equations 2.35 in 2.34 we get:

$$J_{tot} \dot{\omega}_m = T_m + \frac{T_l}{n} - c_{f_{tot}} \omega_m - \tau_{s_{tot}} \operatorname{sign}(\omega_m)$$

(2.36)

where J_{tot}, $c_{f_{tot}}$ and $\tau_{s_{tot}}$ denote respectively, the total moment of inertia and the viscous friction coefficient of the engine-drum group. Their have been defined as follow:

$$J_{\text{tot}} = J_m + \frac{J_l}{n^2}$$
$$\tau_{s_{tot}} = \tau_{s_m} + \frac{\tau_{s_l}}{n}$$
$$c_{f_{\text{tot}}} = c_{f_m} + \frac{c_{f_l}}{n^2}$$

(2.37)

At the kite's operating conditions of interest in the present work, the contribution of the static friction can be neglected, so equation 2.36 reduces to:

$$J_{tot} \dot{\omega}_m = T_m + \frac{T_l}{n} - c_{f_{tot}} \omega_m$$

(2.38)

Figure 2.9: Examples of flexible wings

Equation 2.38 describes the dynamical behaviour of the ground system, composed of the engine, gear-box and drum. In the adopted model, T_m is assumed to be directly controlled i.e., current loop dynamics are neglected for the purpose of this work.

2.4.   Model parameters

Kite

The AWE considered in the present work is of the flexible-wing, soft kite type: they have no rigid structure or support to maintain their shape. The kite inflates with wind pressure and forms an airfoil profile, like the wing of an airplane, which provides substantial lift. Some examples of soft kite are depicted in figure 2.9.

The main parameters set for the simulations are shown in the table 2.2

Table 2.2: Kite parameters

Kite			
Name	**Symbol**	**Value**	**Unit**
Airfoil area	A_a	140	m^2
Projected Area	A	98	m^2
Mass	m	35	kg
Wingspan	d	20.5	m
Aerodynamic lift coefficient	C_L	1	–
Aerodynamic Efficiency	E	6	–

Ground Station

The ground station is composed by mechanical and electrical components. Equipment should be designed to maximize the system performance.

For the transmission a gear ratio n equal to 20 has been assumed.

We then focus on the engine design: we need to choose the right engine for the given AWE set up. For its proper choice we firstly need to compute the maximum power required by the system in nominal condition. Then, taking into account the chosen gear ratio n, the maximum nominal force will give us the required information for the electric machine design.

The theoretical maximum power required by the system was studied by Loyd in [26] and it's equal to:

$$P_{n,max} = \frac{2}{27}\rho A C_l E_{eq}^2 (1 + \frac{1}{E_{eq}})^{\frac{3}{2}} v_{n,max}^3$$

$$E_{eq} = \frac{C_l}{C_{d,eq}}$$

$$C_{d,eq} = C_d(1 + \frac{2rd_t C_{d,t}}{4AC_d})$$

$$v_{n,max} = |W_n \frac{cos(\theta_{Tr})}{3}|$$

(2.39)

where θ_{TR} correspond to the minimum elevation angle reached during the *Traction* phase. In the following computation nominal value of the wind speed magnitude W_n of $12\,\mathrm{m\,s^{-1}}$ has been considered. Moreover, since the kite's *Traction* phase algorithm ensure the system to fly at an elevation of approximately $0.3\,\mathrm{rad}$ (as explained in section 3.1), so this will be the value of θ_{Tr} used to compute the maximum power. To calibrate the power, the *Traction* phase requirement has been considered the most demanding phase.

Considering the safety constant $c_{s,e} = 2$, the required nominal power for tether is given

by:

$$P_{req} = c_{s,e} P_{nom} = 2P_{nom} \tag{2.40}$$

From equation (2.39) a maximum traction velocity $F_{n,max}$, can be computed by dividing the maximum nominal power $P_{n,max}$ by the speed $v_{n,max}$. Then, to compute the torque at the drum side, the drum radius have to be considered. Its cross section radius r_{2cy} is equal to 0.5 m (see table 2.3). From the computation the following desired value of torque on the drum side of the gearbox was obtained:

$$T_d = 11.13 \, \text{kN m} \tag{2.41}$$

Thus the minimal requirement in term of the motor torque T_E is:

$$T_E = \frac{T_d}{n} \tag{2.42}$$

The choice fell on the ABB's model AXR400ML4, from the data sheet [3], it can be verified that the motor power is T_N greater than the required, thus confirming the choice.

$$T_N \geq T_E \tag{2.43}$$

Finally, to design the proper drum mechanical parameters, having fixed its diameter equal to 0.5 m (see table 2.1 in section 2.4), assuming a maximum tether length of 700 m, a diameter of 22 mm (value derived from computations in the follow), the required length for the drum is approximately 5 m.

Table 2.3: Ground Station parameters

Ground Station			
Name	**Symbol**	**Value**	**Unit**
Gearbox ratio	n	20	–
Viscous friction coeff.	C_f	0.8	N s
Maximum torque of motor	T_N	5569	N m
Drum Length	l_{drum}	5	m
Drum radius	r_{2cy}	0.5	m

Tether

The type of tether chosen in this work is the *Dyneema sk78*, a tether of braided ultra-high molecular weight polyethylene characterized by very high breaking load. Other characteristics are low stretch, good resistance to chemicals and UV and improved abrasion resistance. The density of this material is about 980 kg/m^3. In the choice of the tether diameter the tracking force action during the most critical operative conditions has to be taken into account.

Figure 2.10: *Dyneema sk78* cable

Numerical simulations has been employed in this design process; the following conditions has been set for simulations:

$$v = 12\,\mathrm{m\,s^{-1}}$$
$$v_{\text{real-out}} = 3\,\mathrm{m\,s^{-1}} \tag{2.44}$$
$$v_{\text{real-in}} = -2\,\mathrm{m\,s^{-1}}$$

while tether diameters within the range 20 mm-23 mm were considered.

In this design phase it is common to introduce a safety factor: in order to maximize the cable life the requirement in terms of break down force is multiplied by this parameter. Calling it $c_{s,t}$ thus we have:

$$c_{s,t} = \frac{\text{Cable break down force}}{\text{Max Operational Force}} \tag{2.45}$$

From literature [11], [16], [23], and from field experience the value of c_s, t is chosen equal to 3.

Analyzing the breakdown force from *Dyneema sk78* datasheet for cable diameters in the range of 20 mm -23 mm, the choice of a diameter cable of 22 mm was made. In fact, as can be seen in table 2.4, this diameter satisfies the requirement in term of the safety factor $c_{s,t}$ that result to be 3.23 (thus higher than the requested 3.00 value)

Table 2.4: Tether's sizing: Variation of Break down force (F_{br}) with tether diameter (from *Dyneema* datasheet). Computed Maximum force (F_{max}) as a function of tether diameter. F_{br}/F_{max} Ratio.

Diameter	Break Down Force	$c_{s,t} \cdot F_{br}$	F_{max} at *Traction*	F_{br} / F_{max}
20 mm	337 000 N	112 330 N	128 660 N	**2.62** ×
21 mm	379 590 N	126 530 N	130 030 N	**2.92** ×
22 mm	422 000 N	140 670 N	130 480 N	**3.23** ✓
23 mm	456330 N	152 110 N	130 280 N	**3.50** ✓

From the characteristics of the *Dyneema sk78* reported in table 2.5 the parameters required from its modelization (see section 2.2) can be calculated. To compute the elasticity constant of spring in the tether model an averaged E value for the Tensile modulus (see figure 2.5) is computed.

$$E = \frac{109 + 132}{2} \quad [\text{GPa}] \tag{2.46}$$

The spring constant K is computed as:

$$K = \frac{EA}{L} \quad [\text{N}\,\text{m}^{-1}] \tag{2.47}$$

where A is the Cross-sectional area of the cable and L its length.

Table 2.5: *Dyneema* material construction characteristics [5]

UHMWPE	Tensile Strength			Tensile Modulus			Elongation
Fiber Type	N/tex	g/den	GPa	N/tex	kg/den	GPa	to break %
SK99	4.3	48	4.1	159	1.80	155	
DM20	3.2	36	3.1	96	1.08	94	3-4
SK75 SK78	3.4-4.0	38-45	3.3-3.9	112-137	1.26-1.55	109-132	

Knowing the density of the material, the mass M of the cable is easily computed:

$$M = \rho * volume \quad [\text{kg}] \tag{2.48}$$

Table 2.6 summarizes the parameters to be set in the tether model.

Table 2.6: Parameters for the Tether model

Tether			
Name	**Symbol**	**Value**	**Unit**
Diameter	d	22	mm
Spring constant coeff.	K	4.6e7	$\mathrm{N\,m^{-1}}$
Mass	M	260	kg
Drag coefficient	C_d	1	–
Damping constant	C	10e5	$\mathrm{N\,s\,m^{-1}}$
Length	L	700	m
Number of nodes	N	2	–

At the ground stations are mounted sensors such as rotary encoder for measuring tether leght, anemometer to have information on ground wind speed and direction, and at the tether tow point, sensors to measure the tether angle direction. Their specific design is not of specific interest for this work.

2.5. Control Structure

In the previous sections the different component of the system have been analysed separately and physical equations have been developed for each one of them. On the ground level, to manage the tether reeling-in and reeling-out operation there is the "winch-engines" unit system, while the sail flying trajectory is controlled by the KSU. The tether is connecting the two subsystems and allows the force transfer accordingly to the elastic-damped model described in 2.2.

This structure allows for a decoupled control structure for the reeling speed and the flight "trajectory". The quotation marks want to highlight that the term trajectory is used here and in the following sections to indicate the azimuth-elevation displacement of the kite.

2.5.1. Trajectory control

To control the kite during flight, two different control trajectory strategies has been developed: one is based on the concept of velocity angle and is used to fly the kite during the *Traction* phase and the two transition phases, while the second one generates the steering angle based only on the reference values of angle θ.

The main control structure during *Traction* phase is taken from [32], it consists in a cascade control composed by two control loops see figure 2.11: the outer one is responsible

for the trajectory tracking of the kite while the inner loop provides the control steering commands. This control system has been suitably designed for the generation of the eight paths.

The flight of the kite is influenced by variation of the length difference of the two bridle lines (see figure 2.5 and definition of the ψ angle in equation (2.13). The inner loop task is to compute the proper input to the steering unit for the generation of a desired turn angle ψ angle. The outer loop is responsible of the generation of a proper set point of the angle γ, i.e γ_{ref}. As explained in [32] introducing the concept of velocity angle $\gamma(t)$ is possible to control the steering of the wing.

The velocity angle $\gamma(t)$ is defined as the angle between the local north $e_N(t)$ and the projection of the wing's velocity vector $v_P(t)$ onto the tangent plane spanned by the local north and east vectors. The following equation holds:

$$
\begin{aligned}
\gamma(k) &\doteq \arctan\left(\frac{v_P(k) \cdot e_E(k)}{v_P(k) \cdot e_N(k)}\right) \\
&= \arctan\left(\frac{\cos(\vartheta(k))\dot{\varphi}(k)}{\dot{\vartheta}(k)}\right)
\end{aligned}
\tag{2.49}
$$

In (2.49) the four-quadrant version of the arc tangent function shall be used, such that $\gamma \in [-\pi, \pi]$. The velocity angle describes the flight conditions of the wing with just one scalar: as an example, if $\gamma = 0$ the wing is moving upwards towards the zenith of the wind window, and if $\gamma = \frac{\pi}{2}$ the wing is moving parallel to the ground towards the local east. During the kite motion, the *Gamma Estimate block* (see figure 2.11) processes data of sensors on the ground station providing suitable estimations of the angles ϑ and φ allowing and estimate of the velocity angle γ. The *Guidance Strategy block* at the outer level, is responsible to generate the reference velocity angle γ_{ref} according to the desired the path.
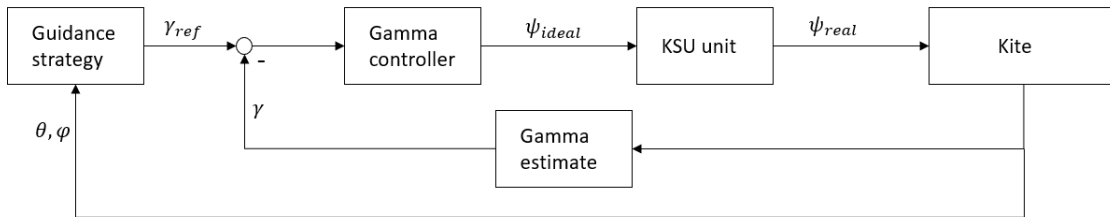

Figure 2.11: γ-controller

In literature difference strategies have been proposed at this scope; in this work the approach proposed in [22] has been adopted. The idea behind this approach is to find a relationship between the turn of the wing and the position of the wing with respect to the ideal path. Each time instant, the reference velocity angle γ_{ref} is generated based on the current position and the on the active target point $P_a = (\varphi_a, \vartheta_a)$. The values of the active target points also change accordingly to the actual phase and to the current position of the kite (see section 3.1). The computed reference velocity angle γ_{ref} is the setpoint of the inner loop that has the so to drive the kite toward it. In [22] the following equation has been proposed:

$$\gamma_{ref} = \arctan\left(\frac{\cos(\vartheta)(\varphi_a - \varphi)}{\vartheta_a - \vartheta}\right) \tag{2.50}$$

Algorithm (3.1) in section 3 illustrates the switching strategy for the definition of the active the target point P_a.

The block *Gamma controller* is implemented as a simple proportional controller.

The *KSU Unit* represents the kite steering unit. This in the simulator is modelled as simple low pass filter characterized by a first order transfer function where the constant τ has been set equal to 0.1. See equation below.

$$G(s) = \frac{1}{(s\tau + 1)} \tag{2.51}$$

The second controller is based on the tracking of the θ angle, this controller is used only during the *Retraction* phase when the kite is in steady state angular position at the border of wind window. The *theta reference* block compute the desired trajectory based on the current position and the reference value. Then the *theta controller* block is a standard PID controller that generate the proper steering command (figure 2.12). More detail can be found in [15].
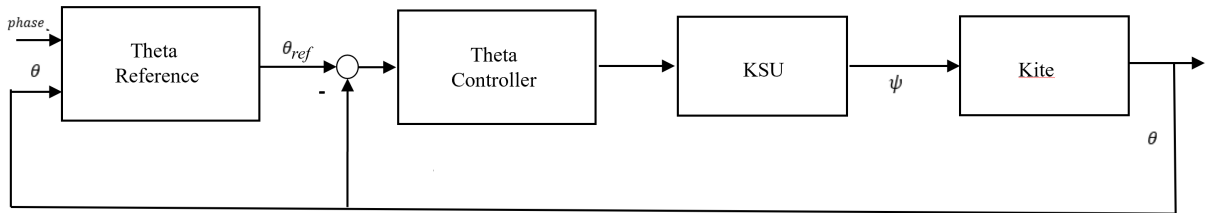

Figure 2.12: θ-controller

In order to prevent the occurrence of windup effects due to the fact that the PID controllers are alternatively activated, a suitable logic has been implemented so to perform what is called "integral tracking".

2.5.2.　Winch control system

As described in section 1.3, in the yo-yo configuration, the kite system alternates between reel-in and tether-out phases to produce energy. Before describing the winch control system we have to obtain the equation that relate the engine-transmission-drum system to the tether. In section 2.3.2 the dynamical equation of the engine-gearbox-drum were derived, here recalled for clarity

$$J_{tot}\dot{\omega}_m = T_m + \frac{T_l}{n} - c_{f_{tot}}\omega_m \operatorname{sign}(\omega_m) \tag{2.52}$$

The torque generated by the drum is only due to its response to the tether. On 2.2 a multi-body modelization of the tether has been illustrated. Considering the tether force at the ground end of the tether and calling it F_t we can write:

$$T_l = F_t r_{2cy} \tag{2.53}$$

where r_{2cy} is the outer radius of the drum.

Considering that the tether reeling speed v_t is related to the angular reeling speed of the drum ω_l by

$$\omega_l = \frac{v_t}{r_{2cy}} \tag{2.54}$$

and considering the gear transmission ratio n defined in (2.35) we obtain:

$$\frac{J_{\text{tot}}\, n}{r}\dot{v}_t + \frac{c_{f_{tot}}n}{r}v_t = T_m + \frac{F_t r}{n} \tag{2.55}$$

Equation (2.55) summarizes the dynamical behaviour of the ground station-tether subsystem.
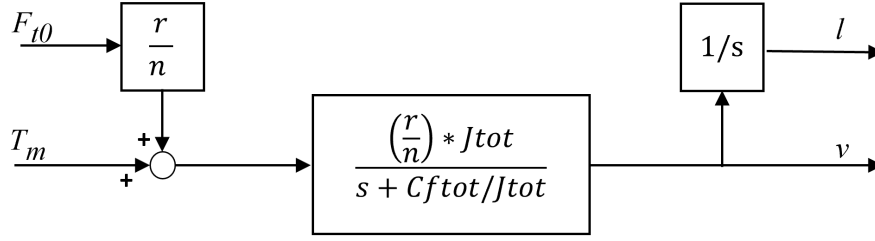
Figure 2.13: Winch system loop system

Considering that

$$\dot{l}_t = v_t \tag{2.56}$$

applying the Laplace transformation to (2.55) we can write:

$$l_t(s) = \frac{\frac{r}{n}}{J_{tot}s^2 + c_{f_{tot}}s}T_m(s) + \frac{(\frac{r}{n})^2}{J_{tot}s^2 + c_{f_{tot}}s}F_t(s) \tag{2.57}$$

The above dynamic equation links the tether length to the torques provided by the engine to the traction exerted by the kite. In 2.13 its schematic representation is depicted. To control the reeling speed of the tether a standard PI Controller as been introduced (see figure 2.14). To implement the controller a discretization of the PI controller has been performed. To prevent windup phenomena due to saturation of the actuator, a proper anti-windup scheme has been adopted.
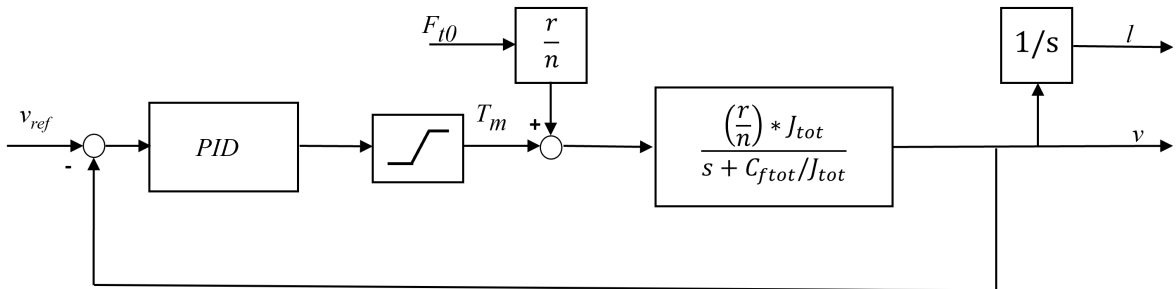
Figure 2.14: Winch system closed loop control system

2.5.3. Supervisor controller

We have described each phase that is part of the production cycle, now we need to create a unique model. To do this, we need to design and implement a supervisory controller

that decides (based on some criteria), which controller will be running at each instant of time. The general structure of this type of controller is presented in figure 2.15. As can be seen in the block diagram, there are lower level controllers and there is a supervisor who is in charge of deciding which of the different controllers is activated and which is deactivated.
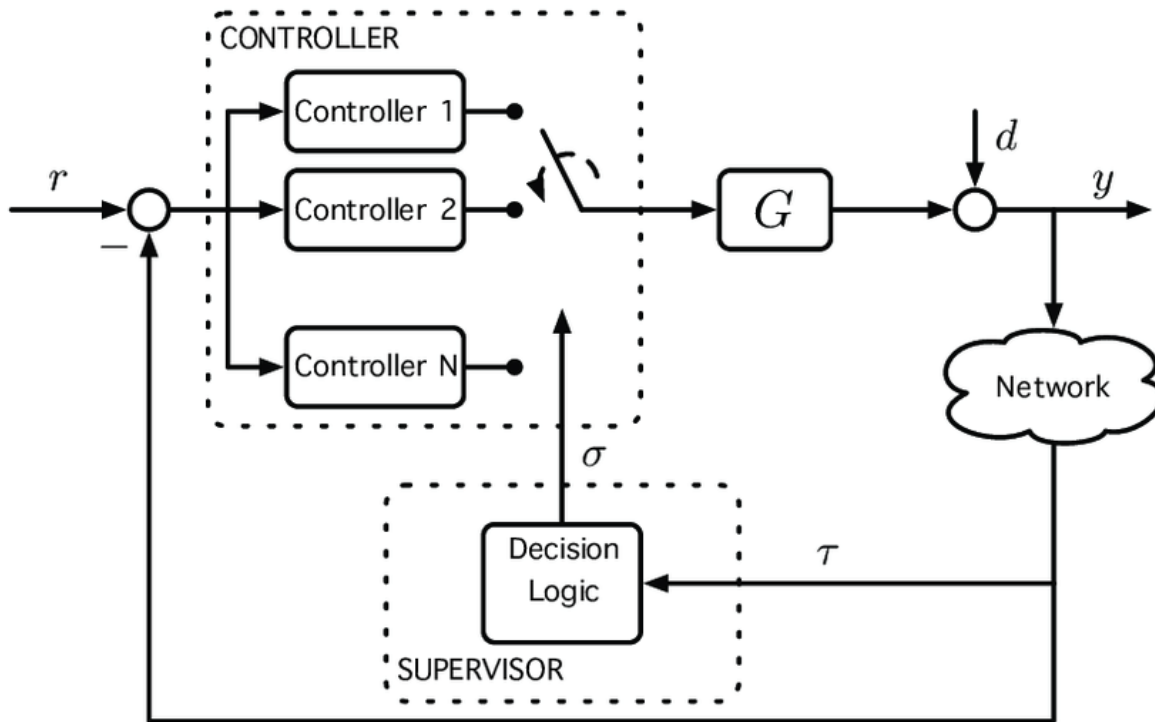
Figure 2.15: A general block diagram of the supervisory control system [14]

The purpose of the supervisor implemented in the simulation is to detect the phases of the kite production cycle in real time. The detection of each phase of the system is based on some switching conditions: the system is in a certain phase until a certain final condition is satisfied, then the system will move to the next phase and so on. Choosing good switching condition between phases is crucial for the good behavior and robustness of the system. Switching conditions between phases will be discussed in more detail in Section 3.1 while here is reported the implemented algorithm:

Algorithm 2.1 Phases supervisor

1: **while** $k < k_{end}$ **do**

2:     $\varphi_{end,Tr} = 0.1$

3:     $\theta_{end,T1} = 1$

4:     $\theta_{end,T2} = 0.3$

5:     **if** $phase(k) = Traction$ & $L \geq L_{end,T1}$ & $|\varphi_{end,Tr} - \varphi| \leq \varepsilon_1$ & $\dot{\varphi} \leq 0$ **then**

6:         $phase(k+1) = Transition\ 1$

7:     **else if** $phase(k) = Transition\ 1$ & $|\theta_{end,T1} - \theta| \leq \varepsilon_2$ **then**

8:         $phase(k+1) = Retraction$

9:     **else if** $phase(k) = Retraction$ & $L \leq L_{min}$ **then**

10:         $phase(k) = Transition\ 2$

11:     **else if** $phase(k+1) = Traction$ & $|\theta - \theta_{end_T2}| \leq \varepsilon_2$ **then**

12:         $phase(k) = Traction$

13:     **else**

14:         $phase(k+1) = phase(k)$

15:     **end if**

16:     $k = k + 1$

17: **end while**

In the algorithm, the ε parameter can be chosen based on the accuracy of the measurement of the θ and the φ angles.

3 | Optimization of cycle parameters

3.1. Production cycle

As previously introduced in section 1.3, the production cycle of the tether kite model consists of four phases. The first phase is the so-called **Traction** phase. Here the tether is unwound to generate energy. During this phase the movement of the kite is controlled to follow a figure of eight path. This type of path is slightly less efficient than a circular loop but is still good at maximizing the generated power and also ensures that the tether does not twist. When the tether reaches a given maximum length, **Transition 1** begins, which is responsible for moving the kite to the side of the power zone, as shown in figure 3.1, where the force is minimal. This maneuver is called *low power maneuver*. Once this position is reached, the **Retraction** phase begins. The system must now consume some energy to rewind the cable. Finally, in order to restart the production cycle, the kite must be brought back downwind and this is the task of **Transition 2**. Now each of the above mentioned phases will be described more in detail, analyzing the key parameters and the initial and final conditions for each one.
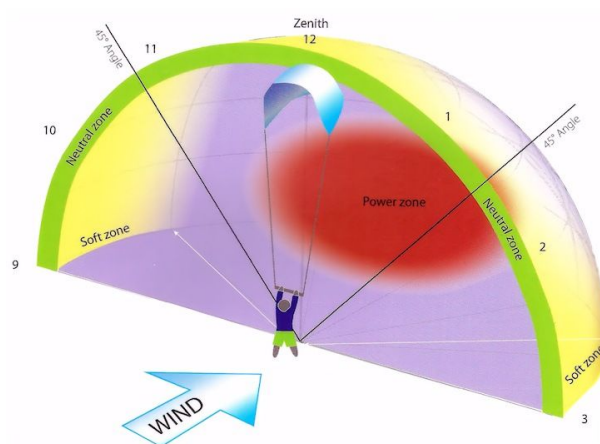
Figure 3.1: The wind window zone. [2]

3.1.1.   Traction

When the *Traction* phase begins the cable is fully reeled-in and the azimuth angle of the kite φ is close to zero, which means it is aligned with the wind. The elevation angle θ is close to the value the kite will maintain during the entire phase. This value is a design choice and is the trade-off between two considerations. The first takes into account the fact that, in order to maximize the force on the sail, the elevation angle should be equal to zero, ensuring that the kite's sail is perpendicular to the wind that blows horizontally. The second consideration is to keep the kite far enough from the ground and avoid collisions. The flight loop trajectory follows an eight-figure up-loop path, eight-figure refers to the shape of the trajectory while up-loop means that the kite is ascending on the outside of the trajectory and descending while on the inside.

In the previous chapter, the guidance strategy was described and the equation that allows the computation of the velocity angle based on the current target point reference and the position was introduced. The advantage of this structure is that it allows to maneuver the kite avoiding the need to precompute an entire trajectory to use as a reference. This is done through a bang-bang type strategy that was introduced by [19] and later developed by [22]. The strategy developed by Fagiano also provides an intuitive link between the control parameters and the position of the resulting paths in the wind window. In this approach two fixed reference points in the plane (θ, φ) are defined, denoted $P_- = (\theta_-, \varphi_-)$ and $P_+ = (\theta_+, \varphi_+)$, with $\varphi_- < 0$, $\varphi_+ > 0$ and $\theta_- = \theta_+$. The controller computes a new value of the reference velocity angle at discrete time instants. At each time step $k \in Z$, one of the two reference points is set as the active target $P_a(k) = (\varphi_a(k), \theta_a(k))$, according to a switching strategy that is described in algorithm 3.1. Thus, the reference

---

Algorithm 3.1 Active TP for Eight-figure trajectory

1: **while** $phase = Traction$ **do**
2:    **if** $\varphi(k) < \varphi_-$ **then**
3:        $P_a(k) = P_+$
4:    **else if** $\varphi(k) > \varphi_+$ **then**
5:        $P_a(k) = P_-$
6:    **else**
7:        $P_a(k) = P_a(k-1)$
8:    **end if**
9: **end while**

---

point is switched when the measured value of φ is outside the range $[\varphi_-, \varphi_+]$. Because of the way we defined the velocity angle γ, after the target point is switched, the wing will start to turn under the action of the internal control loops, following up-loops. The main parameters to be chosen in the described guidance strategy are the target points P_- and

P_+. Choosing these points is out of the scope of this work and the parameters used are taken from [15]. The values are $P_+ = (0.3, 0.3)$ and $P_- = (0.3, -0.3)$.

It's worth to recap that using precomputed reference trajectories based on some mathematical model of the system, would cause an inevitable issue with model mismatch and approximation that could give rise to problems related to the stability and attractiveness of the chosen trajectory. The implemented solution, on the other hand, is much more robust and does not rely on any measurement or estimation of the wind speed. The only assumption needed is that the interval $[\varphi_-, \varphi_+]$ must be centered around the wind direction.

Moving on to the winch controller, it is clear that the main variable to be tuned for this phase is the reeling out speed of the tether. Different speeds highly affect the resulting average cycle power. Indeed, the reeling out speed influences the average power production both directly and indirectly. The instantaneous power is proportional to the reeling speed but at the same time a higher reeling speed would cause a lower force acting on the wing, since the local apparent wind would drop. Some results can be found in the literature in order to set this speed based on the nominal wind speed, however since this value is often not available or inaccurate, an approach like the one of [9] can be used to determine the proper reeling speed based on the measure of the force acting on the tether. When the cable reaches the defined maximum length the next phase starts.

3.1.2. Transition 1

In most of the literature, *Transition 1* begins when the maximum tether length is reached. This is due to the fact that then the tether is locked and the kite is flown out of the wind. However the optimal solution that maximise the average power production over the entire duty cycle, found by this work, shows that it's convenient to reel out some extra cable while moving out of the power zone. In this way, the tether is not subject to sudden force peaks and the overall cycle efficiency is maximised.

If the switching condition is based on reaching a certain cable length, the kite's initial position is at $\theta \approx 0.3$ and $\varphi \in [\varphi_- \varphi_+]$. However, in order to be able to compare the optimal trajectory found by the optimizer, the initial position in the eight-figure path has to be the same for each cycle. Thus, the implemented switching condition forces the tether to reach a given minimum switching length length and to have a fixed azimuth and elevation when switching from *Traction* to *Transition 1*.

The guidance strategy used here is the same one used during the previous phase. The velocity angle γ is computed based on the current (θ, φ) tuple and on the active target point $P_a(k)$. The difference lies in the switching algorithm for the target points. In

fact, the path to be followed by the kite will be an arc of curve and not an eight-figure. The algorithm is described in 3.2. The idea behind it is really simple: when one target point is reached the next one becomes active. As it can be seen, the switching condition implemented in algorithm 3.2 is only on the elevation angle θ. This is due to the fact that imposing a switching algorithm with a condition on both θ and φ would increase the risk of obtaining undesired behaviour of the kite's trajectory. For example, if the kite exceeded the φ angle of the active target point before reaching the theta angle, then the kite would reverse its course to reach the elevation necessary for the corresponding azimuth and then move to the next TP and reverse flight direction again. This is clearly an undesired behaviour that would slow down the maneuver and cause troubles. The kite should just move on to the next TP until it smoothly reaches the final position of the transition.

Algorithm 3.2 Switching Reference TP Algorithm

1: **if** $phase = Transition1$ **then**
2:    $err_\theta(k) = |\theta(k) - \theta_{ref}|$
3:    **if** $err_\theta(k) < \varepsilon$ **then**
4:       $TP_\theta = TP_{\theta,next}$
5:       $TP_\varphi = TP_{\varphi,next}$
6:    **else**
7:       $TP_\theta = TP_{\theta,old}$
8:       $TP_\varphi = TP_{\varphi,old}$
9:    **end if**
10: **end if**

The reeling speed of *Transition 1* is the most crucial aspect and the solution proposed is one of the main contributions developed within this work. Two different control logic have been implemented in order to guarantee a long life of the components (avoiding sudden force peaks on them) and to obtain a smooth and efficient transition from the reeling-out to the reeling-in reference speed. More details will be given in the next sections. However, it can be anticipated that the winch controller, in this phase, has to follow a slowly varying reference speed. To start the next phase the system has to reach the steady state position at the edge of the wind power zone at the desired elevation. More precise explanations on the final switching conditions can be found in the next section, as this is also the desired starting condition of the *Retraction* phase.

3.1.3. Retraction

Once the kite has reached the desired position, i.e. it has moved to the side of the power zone, the *Retraction* phase begins. Here, the force acting on the kite is low and the energy consumed to retract the cable is minimal. In terms of elevation and azimuth position this corresponds to angles equal to $\theta = \frac{\pi}{2}$ and $\varphi = \pm\frac{\pi}{2}$. Note that when the kite is exactly above the ground station ($\theta = \frac{\pi}{2}$) the azimuth angle of the point-to-mass modeled kite "loses meaning", any value would correspond to the same point. This could create problems for the angle measurement and may even lead to situation where the cable is likely to twist. Additionally, the control sensitivity is low.

At an angle of $\varphi = \pm\frac{\pi}{2}$ the wind hitting the sail is also low but the sensitivity of the control is higher. Furthermore, if we suppose, for example, to have a $700\,\text{m}$ long cable and start the *Retraction* phase at a position with ($\theta = 1, \varphi = \frac{\pi}{2}$) compared to a position with $\theta = \frac{\pi}{2}$, the height of the kite from the ground would be about $110\,\text{m}$ lower. Having stated at the beginning of this work that the wind grows with increased height from the ground, it would be a contradiction to decide to move out of the wind but at the same time move to a sensibly higher height without having concrete advantages.

The need to introduce a different control strategy is given by the fact that during this phase the velocity angle γ as computed in (2.49) becomes undefined, so that this variable is not representative of the wing's orientation anymore and cannot be used for feedback control. Indeed, during the *Retraction* phase, the wing's velocity is low and its main contribution is given by the reel-in speed. Indeed, the component of the wing's velocity perpendicular to the line direction is close to zero and the apparent wind speed is determined only by the wind speed W and the reel-in speed $\dot{r}$ [32].

The winch controller during this phase behaves similarly to the *Traction* phase. The reference speed of the winding is constant and its value affects the efficiency of the system. The differences lie in the fact that here energy is being consumed since the reeling speed is negative. In this phase the aim is therefore to minimize the energy consumed but at the same time minimize the transition duration. At the end of this phase, all the tether has been rewound and the kite is positioned on the edge of the power zone. Then *Transition 2* starts and brings back the kite to the proper position so that a new production cycle can begin.

3.1.4. Transition 2

At the beginning of this phase the kite has an elevation of $\theta = 1[rad]$ and an azimuth of $\varphi = \pm\frac{\pi}{2}$. The situation is as follows: the tether has reached the minimum length, but with

a wrong position to start the next cycle. The kite has an elevation of $\theta = 1[rad]$ and an azimuth of $\varphi = \pm\frac{\pi}{2}$. *Transition 2* allows the kite to return to its starting point to start the cycle again. Also for the *Transition 2* we decided to use the trajectory controller based on the velocity angle γ. The alternative solution would have been to design a controller based on the *theta* elevation angle as in the *Retraction* phase. However, it was decided to use the first method because it is more reliable and during the *Transition 2* the velocity angle γ is well defined.

During *Transition 2* the tether is neither reeled in or out as it used to be done in the previous approach for the *Transition 1*. This, as already discussed for *Transition 1*, causes increased stresses on the tether and the wing. However since at the beginning of the transition the kite is out of the wind, the forces in place are significantly less than during *Transition 1*. This implies that there is no potential risk to the life expectancy of the components. The transition normally takes a very short time and ends when the kite is positioned at the correct azimuth and elevation to begin the new cycle.

3.2.   Optimization Problem setup

Let's now get into the focus of this thesis in more detail, i.e. start to better understand which are the guiding ideas that shape the work. The goal of this work is to find an optimal trajectory for the *Transition 1* that is independent from the nominal wind speed, and to design a control strategy that allows to avoid abrupt changes in force during the transition from the *Traction* phase to the *Retraction* phase.

As stated, when the controller model was introduced in section 2.5, the reeling velocity control structure and the θ-φ trajectory planning can be designed separately one from the other. However the optimal solution that maximises the average power of the production cycle needs to take into account the kite's winch controller performance in order to determine the optimal θ-φ trajectory. Now let's have a look on a few physical equations to get a better grasp of the situation. The average cycle power is given by the the integral over the time of the product between the force and the reeling speed, divided by the duration of the cycle itself..

$$P_{avg} = \frac{1}{T} \int_0^T T_m(t)\omega_m(t) \, dt = \frac{1}{T} \int_0^T F_{t0}(t)\dot{r}(t) \, dt \tag{3.1}$$

In first approximation, the force acting on the tether is given by the following equation:

$$F_{t0} = C(r)\left(W\cos(\theta)\cos(\varphi) - \dot{r}\right)^2, \tag{3.2}$$

where $C(r)$ is a parameter that depends non-linearly on the length of the tether reeled out, W is the nominal wind and $\dot{r}$ is the reeling speed (see [24] for further details). For the scope of this section $C(r)$ can be considered constant. Equations (3.1) and (3.2) describe how a change in the reeling velocity or in the position of the kite affects the force and the power.

3.2.1. Winch control structure

As stated before, the goal for the winch controller implemented here is to avoid peaks in the force acting on the wing and on the tether. However the overall goal should not be forgotten: maximising the energy production. Before proceeding to illustrate the implemented solutions, let's make some brief considerations:

- Until the reeling speed is positive the system is producing energy, when it's negative energy is consumed.

- Since the wind is considered to blow horizontally the forces are maximal for both elevation and azimuth angle of $0\,\mathrm{rad}$ and minimum at $\frac{\pi}{2}$ rad (see eq. (3.2))

Therefore a possible idea could be to let the cable unwind while the kite is moving out of the wind and start to reel-in when it has reached the starting position of the *Retraction* phase. However, this solution is clearly not optimal. Beside the fact that if the forces become too low the kite could fall ruinously to the ground, a lot of extra cable would be reeled-out while being out of the wind, decreasing the efficiency of the system.

The preceding statement is intended to bring out a concept: the fact that the *Transition 1* does not have to be intended neither as a production phase nor as a phase that only consume energy. The right interpretation is to look at it as a "transition phase", meaning that some energy will be produced and some consumed and the main goal is to minimize the time spend at *Transition 1* and to bring the kite from the previous phase to the next one. The reasons for this are simple. One is that the system is most efficient in producing energy during the *Traction* phase, when the kite is downwind. The other is that the system minimises the energy used for the winding operation during the *Retraction*, when the kite is out of the wind.

Starting from these considerations and the knowledge acquired through different attempts, the idea used to implement the winch controller structure is the following. The force on the cable, if the reeling speed is constant, decreases as the kite moves out of the wind. While the reeling speed is positive it would be desirable to have an high force, where high means a value comparable to the one of the *Traction* phase. Thus, the reeling speed $\dot{r}$ could be decreased in order to compensate for the reduced force due to the the kite sliding

out of the wind.

Force Estimate Strategy

In order to obtain an estimate of how much the reeling speed $\dot{r}$ should decrease in order to keep the force on the tether constant, equation (3.3) can be used.

$$\dot{r} = W\cos(\theta)\cos(\varphi) - \sqrt{\frac{F_{t0,ref}}{C}} \tag{3.3}$$

This requires the measurements of the nominal wind speed W, the elevation angle θ and the azimuth angle φ to be available.

Algorithm 3.3 summurizes the proposed control strategy. To understand this algorithm, let's recall the control structure of the winch, described in section 2.5. The low level controller is a reference tracking PI controller implemented with an anti wind-up structure, while the higher level controller is a switching controller that sets the desired reference v_{ref}.

Algorithm 3.3 Winch Controller Supervisor Logic - Force Estimation Strategy

1: **if** $phase_{old} = Traction$ & $phase = Transition\ 1$ **then**
2:      $F_{t0,ref} = F_{t0}(k)$
3: **end if**
4: **if** $phase = Transition\ 1$ **then**
5:      $v_{ref}(k) = W(k)\cos(\theta(k))\cos(\varphi(k)) - \sqrt{\frac{F_{t0,ref}}{C(r)}}$
6:      $v_{ref}(k) = \max(v_{retraction}, v_{ref}(k))$
7: **end if**

As it can be seen above, at each time step the reference speed $v_{ref}(k)$ is computed and given as input to the low level controller. The max function used in line 6 ensures that the the reference speed does not get lower than the optimal reeling speed of the *Retraction* phase. The reference value of the force $F_{t0,ref}$ is chosen dynamically, based on the force acting on the tether when *Transition 1* starts. In this way we can ensure that the reference value is reasonable and that the computed $v_{ref}(k)$ behaves smoothly.

The measurements of the force F_{t0} and the angles θ and φ are obtained with a good accuracy by the sensor on the GU, however, that's not true for the wind measurements. In a real scenario the wind is measured through some sensors (e.g. an anemometer) at ground level. To determine the wind speed and direction at wing attitude, atmospheric models, such as the wind shear model, can be used. Due to the limited accuracy, wind speed cannot be used as a feedback variable by the winch controller, which is the major

drawback that limits potential real world applicability of this strategy [21]. This lead to the implementation of the next approach.

Saturated Control Action Strategy

The goal of this implementation is the same of the previous one, i.e. to reduce the reeling speed in order to keep the force on the tether in the desired range, ensuring that no abrupt changes on its values occur. In this new strategy the nominal wind speed is considered not available, so no variable set point of the reel-in speed is generated but, in order to achieve similar results as respect to the control strategy discussed in the previous section, the structure of the controller is modified.

The control scheme for the speed reference tracking can be seen in figure 2.14. The difference w.r.t. the version implemented previously lies in the values of the saturation of the control action. This value is computed based on the measure of the force acting on the cable at the switching instant between the *Traction* phase and the *Transition 1* (line 2 of the algorithm 3.4). Then the corresponding mechanical torque is calculated in line 3 by multiplying the force $F_{t0,ref}$ by the radius of the drum r_{2cy} and dividing by the gearbox ratio n. This torque values is used as the saturation values of the control action during the entire transition. In this way we can guarantee that the force on the tether does not exceed reference values.

The reference speed v_{ref} is set equal to the one of the *Retraction* phase. Since at the beginning of the *Transition 1* the actual value of the reeling speed is far from the selected v_{ref}, this causes the PI Controller to generate a high torque request to the actuator. The saturation value imposed severely limits the actual actuator torque guaranteeing the desired smooth force trend. This results in the desired reeling speed profile, as shown in figure 4.8 . This profile is obtained thanks to the fact that the forces decrease while moving out of the wind and the saturated control action.

Algorithm 3.4 Winch Controller Supervisor Logic - Saturated Control Action Strategy

---

1: **if** $phase_{old} = Traction$ & $phase = Transition\ 1$ **then**

2:     $F_{t0,ref} = F_{t0}(k)$

3:     $T_{m,max} = F_{t0,ref} \frac{r_{2cy}}{n}$

4: **end if**

5: **if** $phase = Transition\ 1$ **then**

6:     $v_{ref}(k) = v_{retraction}$

7: **end if**

It's important to notice that this strategy has the advantage of not requiring the wind

speed to be known, however it also has a drawback. Looking at the control scheme in figure 2.14, it can be noticed that by imposing the artificial saturation to the control action and giving a reference speed that saturate it, the system is basically an open-loop system whose output depends only on the disturbance F_{t0}. From a control point of view this would clearly seems as a mistake since the system would not be able to react if the disturbance F_{t0} increases. One could argue that this only works as we are in an ideal condition where the wind is constant and the values of F_{t0} always decrease while we move away from the wind. However from a practical point of view the controller's inability to compensate for an increase in the disturbance is acceptable or rather desirable: a sudden rise of the disturbance F_{t0} (e.g. a gust of wind) would lead to reel-out some extra meters of cable instead of exposing it to high stress.

3.2.2. Trajectory Optimization

Now that the two control strategies have been explained the trajectory optimization problem can be formulated. The goal is to find the optimal sequence of target points, and by extension the optimal trajectory that maximises the average power production at different wind speeds. As introduced in section 3.1 in the *Transition 1* section, the switching condition for the start of the *Transition 1* has been chosen to ensure that the kite is always in the same location of the eight-figure path. This choice allows to compare the results obtained by repeating the optimization routine with different wind speed.

Optimal problem formulation

The nonlinear trajectory optimization problem can be solved through constrained nonlinear optimization routines. The chosen algorithm is BFGS, and the central difference method is used to calculate the gradient. The aim is to find the four target points Q_{t1} and the optimal reeling speeds v_{reel}. Each TP is defined in terms of an elevation and azimuth angle $Q_{t1}(i) = (\theta_i, \varphi_i)$, while v_{reel} is defined in term of two reeling set points: one for the *Traction* and one for the *Retraction*, $v_{reel} = [v_{traction}, v_{retraction}]$.

Since we are dealing with a quite complex-nonlinear problem the solver will not find a solution under random initial conditions. A reasonable starting point is needed. For this reason the Q_{t1} are initialised at equidistant angles varying from the *Transition 1* initial switching conditions to the final switching conditions. Moreover the initial reeling speed are initialised accordingly the results found in [15] for each one of the nominal wind speed conditions considered. Moreover several linear constraints had to be added in order to allow the controller to find a solution.

In the cost function the average power P_{avg} is maximised and its values is computed as:

$$P_{avg}(Q_{t1}, v_{reel}) = \frac{1}{T} \sum_{k=0}^{T} T_{m_k}(Q_{t1}, v_{reel}) \omega_{m_k}(Q_{t1}, v_{reel}) \tag{3.4}$$

Then the optimization problem can be written as follows:

$$\max_{Q_{t1}, v_{reel}} P_{avg}(Q_{t1}, v_{reel})$$

$$\textbf{s.t.}$$

$$0.3 \leq \theta_i \leq 1 \quad with \; i = 1 \ldots N - 1$$

$$\theta_i \leq \theta_{i+1} \quad with \; i = 1 \ldots N - 1$$

$$\theta_{ref_{t1}} \leq \theta_N \leq \frac{\pi}{2}$$

$$-\frac{\pi}{2} \leq \varphi_i \leq \frac{\pi}{2} \quad with \; i = 1 \ldots N \tag{3.5}$$

$$\varphi_i \leq \varphi_{i+1} \quad with \; i = 1 \ldots N - 1$$

$$0 \leq v_{traction} \leq v_{traction,MAX}$$

$$v_{retraction,MIN} \leq v_{retraction} \leq 0$$

$$F_{t0}(Q_{t1}, v_{reel}) \leq \frac{F_{tether_{MAX}}}{c_{s,t}}$$

where N is the number of target points, and is set equal to 4. The nonlinear constraint on the tether force is bounding the force to be $c_{s,t}$ times smaller or equal the maximum force to which the cable may be subjected without braking. The breaking force $F_{t0_{MAX}}$ is computed as function of the tether diameter and $c_{s,t}$ is set equal to 3 as this factor ensure the maximum lifetime of the tether (as explained in section 2.4).

4 | Simulation results

In this chapter the results of the optimization routines will be shown and then analysed in order to understand them better and draw conclusions.

First of all, let's introduce the benchmark that will be used in the next pages to evaluate the solutions presented. The results obtained are computed by running the simulation in the following conditions:

- During the *Transition 1* the v_{ref} given as reference to the low level winch controller is imposed equal to 0.
- During the *Transition 1*, a unique target point Q_{t1} is given as reference to the guidance system. The values is set equal to $\left(\frac{\pi}{2}, \frac{\pi}{2}\right)$.
- Optimal reeling velocities v_{reel} varies with the wind intensity, the same values are used for both the benchmark and the optimized results. Doing so ensures that the results presented are not biased by this sensitive choices.
- Nominal wind speed is set equal to $W = 12[m/s]$ as this was the wind intensity on which the the design choice reported in section 2.4 were made.
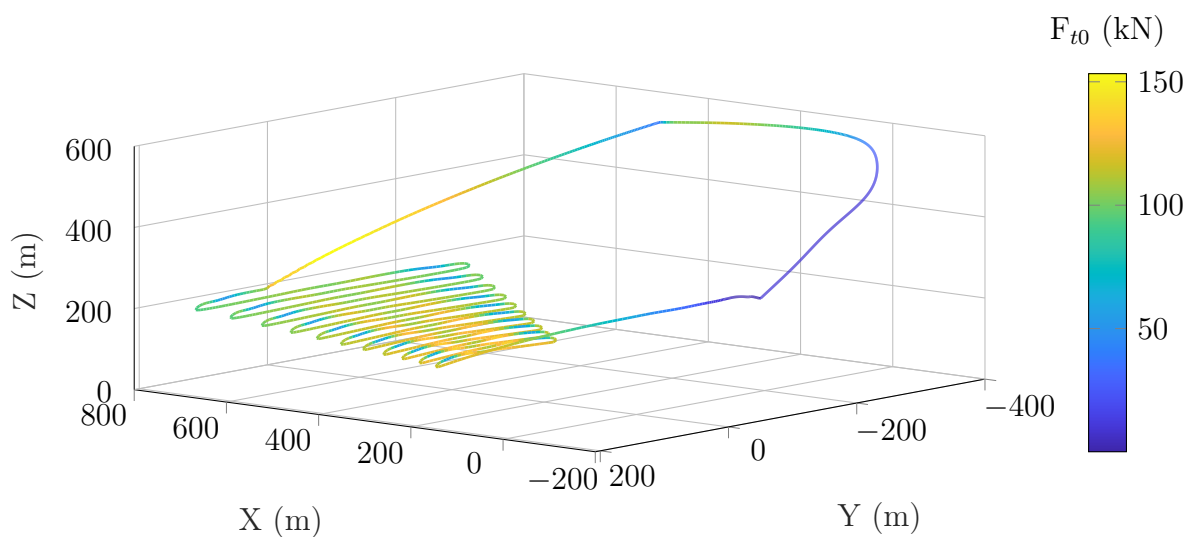
Figure 4.1: Kite's 3-dimensional trajectory corresponding to the benchmark approach, the force acting on the tether is color coded

Table 4.1: Main system parameters used in the simulation.

System Parameters			
Name	**Symbol**	**Value**	**Unit**
Kite projected area	A	98	m^2
Kite wingspan	d	20.5	m
Tether diameter	d	22	mm
Tether break down force	F_{br}	422 000	N
Tether safety factor	c_{st}	3	–
Tether length	L	700	m
Gearbox ratio	n	20	–
Electric machine nominal torque	T_N	5569	N m
Winch drum radius	r_{2cy}	0.5	m

In the table above the main system parameters used in the simulation are shown. More details can be found in section 2.4

The 3-dimensional plot in figure 4.1 shows the trajectory followed by the kite during an entire cycle while the force acting on the tether F_{t0} is color coded. Blue dashes represent forces in the order of $20\,kN$ while yellows correspond to values over $140\,kN$. Right after the kite ends the eight-figure path entering the *Transition 1*, the force rises quickly until it reaches the yellow peaks. Figure 4.2 shows the force trend in time: on the left the entire cycle is shown and on the right the focus is given to *Transition 1*.
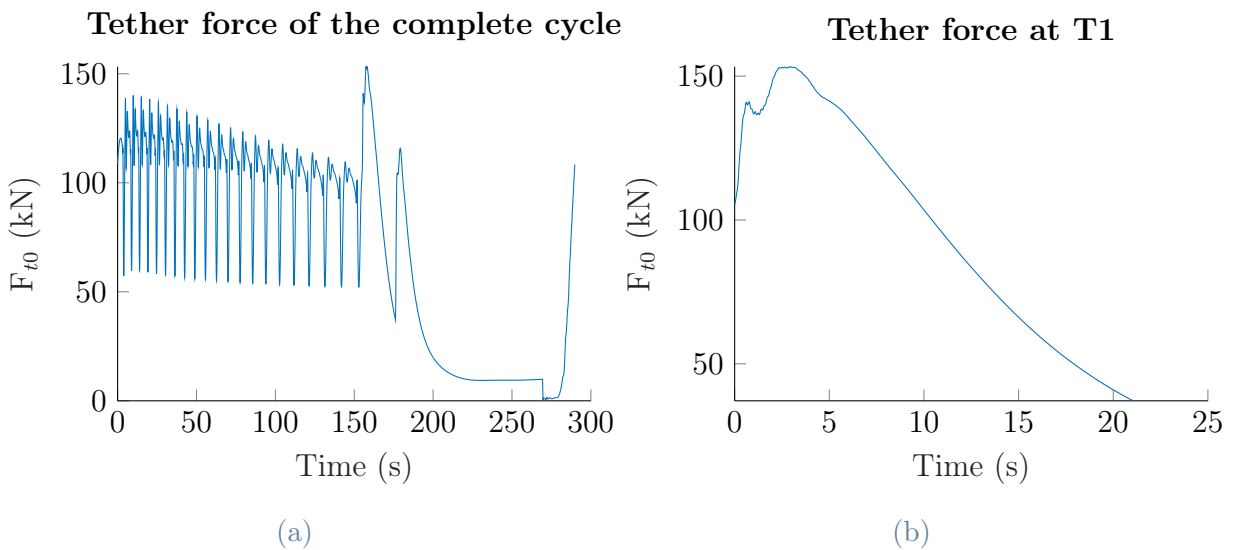
Figure 4.2: The force in the benchmark simulation acting on the tether during the entire cycle (a) and during the interval of *Transition 1* (b).

The peak value reached by the force on the tether is higher than the value obtained by dividing the tether break down force by the safety factor, i.e. grater then 140 kN (see table 4.1). Staying beneath this value means ensuring the desired cable lifetime. Thus, repeating this cycle several times per hour would soon result in significantly higher cable wear and therefore higher maintenance costs.

4.1.   Winch control strategy for Transition 1

As stated in section 2.5 the goal of the implemented control strategy is to ensure a smoother behavior of the force acting on the tether during the *Transition 1*. Therefore, in the next subsections the trends of the tether force F_{t0} obtained with the different winch control logic will be compared to the benchmark approach. Let's recall that in the benchmark approach the winch controller reference speed v_{ref} is set equal to 0.

4.1.1.   Force estimate strategy

This implementation is exploiting the knowledge of the wind intensity in order to compute the speed v_{ref}, ensuring that the desired force acts on the tether. v_{ref} is given as a reference to low level winch controller accordingly to equation (3.3).
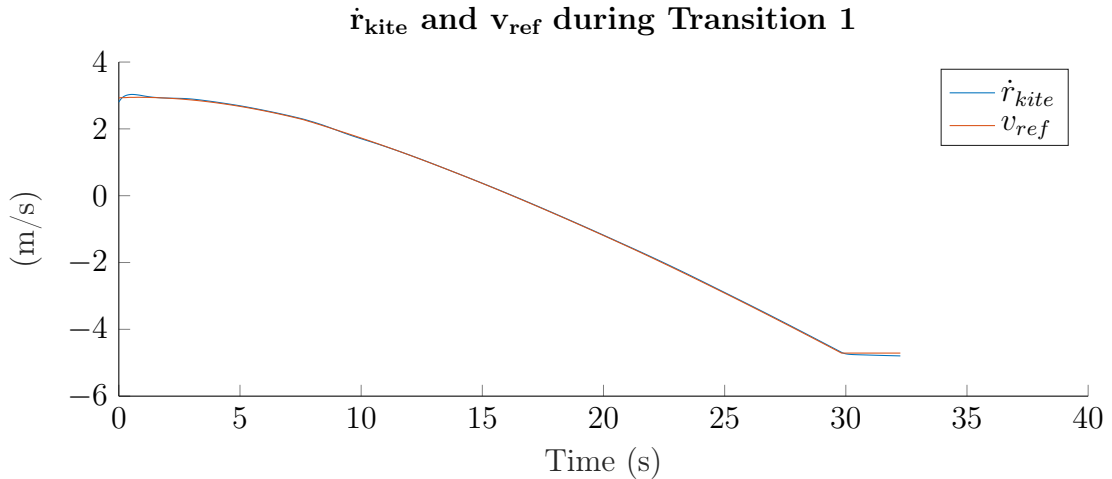
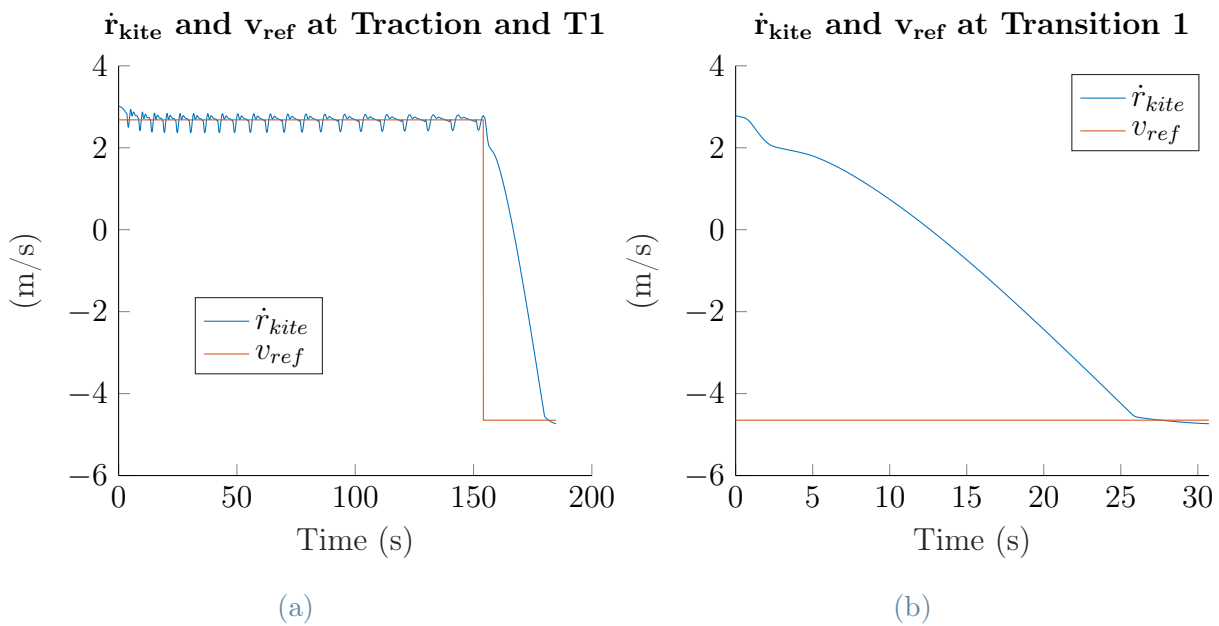

Figure 4.3: Comparison of the winch controller reference with the "force estimate strategy" and the actual tether speed during *Transition 1*.

In figure 4.4 and in figure 4.5 a satisfactory behaviour of F_{t0} is shown, the force no longer increases but instead remains constant until the reeling velocity reaches the set point value of the *Retraction* phase.

Looking at figure 4.5, it can be seen that after about 30 seconds, from the start of the *Transition 1*, the force begins to decrease. This occurs because the $\dot{r}$ required to guarantee the value of $F_{t0,ref}$ is lower than $v_{retraction}$ (equation (3.3)) but the winch controller reference v_{ref} can not be smaller then $v_{retraction}$ (see algorithm 3.3, line 6). A verification of what has just been asserted can be seen in figure 4.3, where the red line represent the reference speed v_{ref} given to the low level controller, and the blue one is the measured speed.
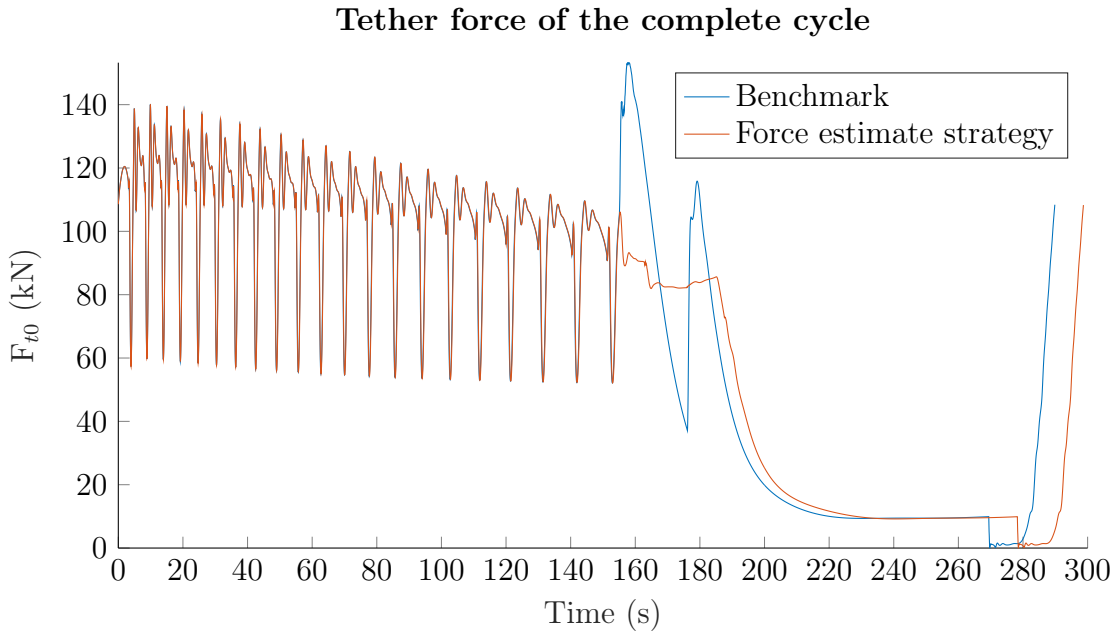
Figure 4.4: Comparison of force acting on the tether during the entire cycle with the original winch control implementation and with the so called "force estimate strategy".
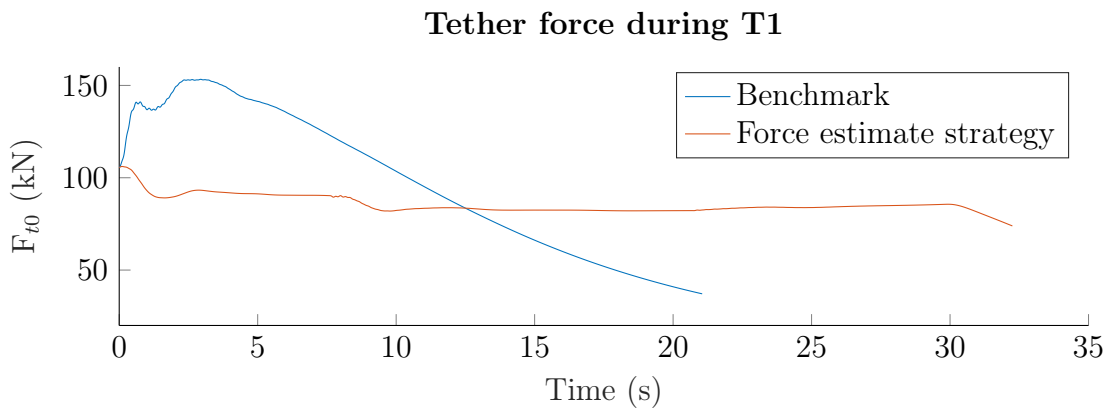
Figure 4.5: Comparison of force acting on the tether during the *Transition 1* with the original winch control implementation and with the so called "force estimate strategy".

4.1.2. Saturated control action strategy

As already pointed out in the previous chapter, the solution proposed above cannot be implemented in a real system due to fact that the wind measurement at the kite's altitude is not accurate. Thus a second strategy was developed. Let's recall that in this solution the winch reference speed v_{ref} is imposed equal to the set point of the *Retraction* phase as soon as the *Transition 1* starts. Then, in order to avoid a situation similar the one of the benchmark case, the control action is saturated at a specific value that ensure the desired behaviour of the force (see algorithm 3.4).

The yellow curve in figure 4.6 and 4.7 illustrates the behaviour of the "saturate control strategy" with respect to the other one previously introduced.

As noticed before in figure 4.5, also in 4.7 can be seen that the force is kept almost constant for most of the transition. Then this values start to drop (around the 26th second from the transition start). With the current implementation, the situation is slightly different from what has occurred previously. In this case the reference has no lower limit, since it is a constant value. But it is the controller that is no longer saturated, since the tracking error is close to zero. A proper implementation of the anti wind-up is essential here to avoid subdelongation, see 4.8 (b).

Tether force of the complete cycle
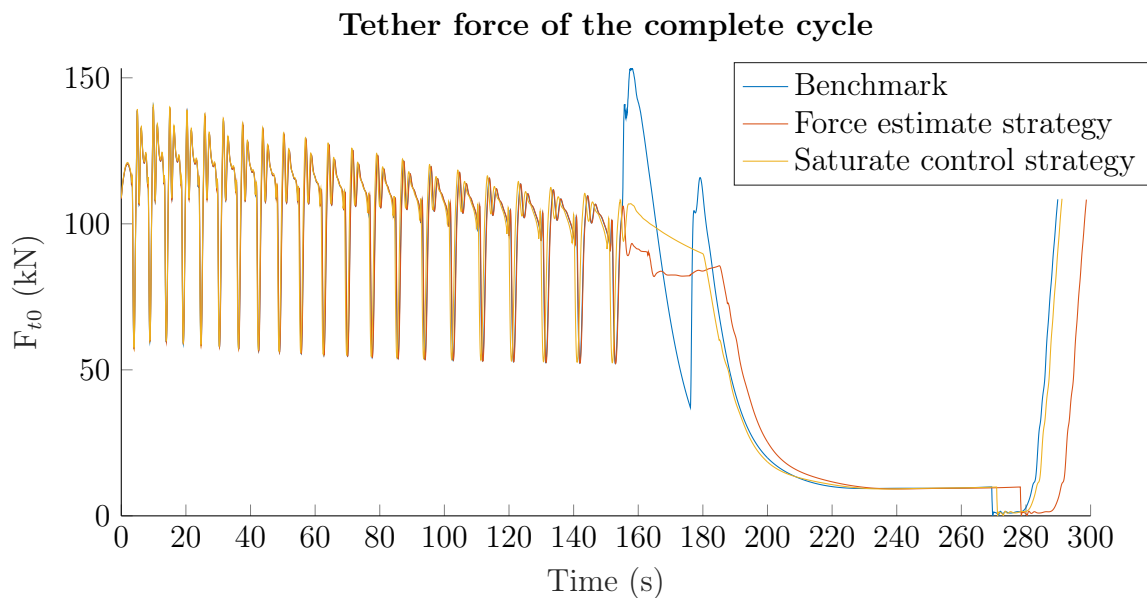
Figure 4.6: Comparison of force acting on the tether during the entire cycle with the original winch control implementation, the so called "force estimate strategy" and the "saturated control strategy".

Tether force during T1
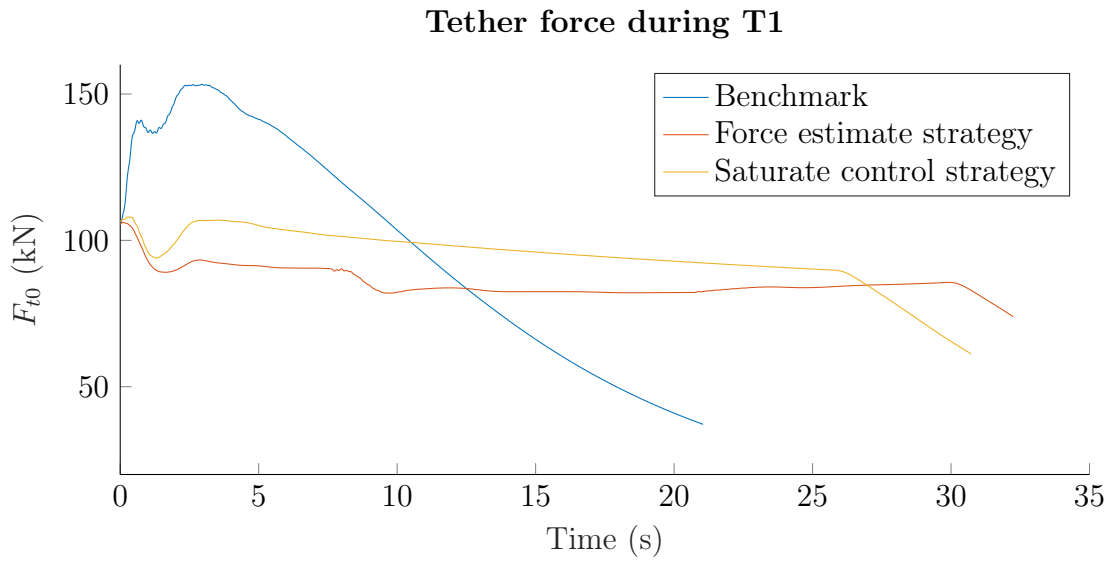
Figure 4.7: Comparison of force acting on the tether during the *Transition 1* with the original winch control implementation, the so called "force estimate strategy" and the "saturated control strategy"".

Figure 4.8: Comparison of the winch controller reference with the "saturated control strategy" and the actual tether speed during: *Traction* and *Transition 1* (a); only *Transition 1* (b)

4.2. Trajectory optimization of Transition 1

Here the results of the optimization problem of are shown. The solutions will firstly be analysed for the case of $W = 12\,\mathrm{m\,s^{-1}}$ and then one unique sub-optimal solution will be obtain independent from the wind speed wind speed.

4.2.1. Optimal trajectory

The optimal solution found by the algorithm at $W = 12\,\mathrm{m\,s^{-1}}$ impose a reference reeling speed values for the *Traction* and the *Retraction* equal to: $v_{reel} = [2.7; -4.7]$. The trajectory is described by the four optimal target point found by the routine that are listed in the table below.

	θ	φ
1	0.3156	0.1848
2	0.4761	0.7933
3	0.7821	0.8531
4	1.0823	1.5708

Table 4.2: Optimal target points

Kite trajectory of the complete cycle
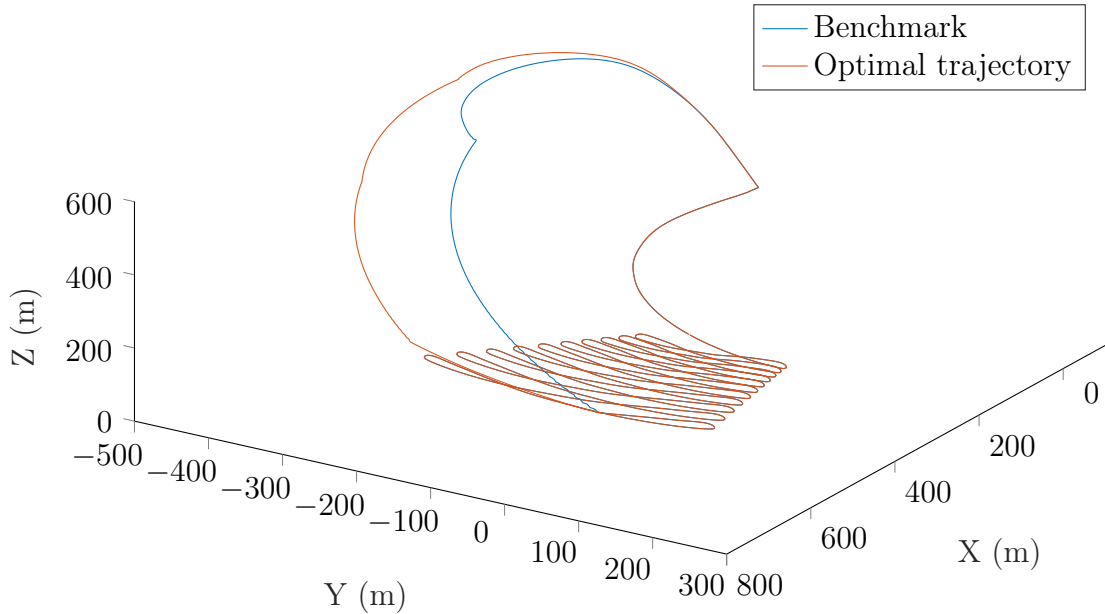
Figure 4.9: The kite's 3D trajectory comparing the benchmark and the optimal simulations.

First let's analyze how the optimal trajectory changes from the one used as a benchmark. Figure 4.9 and 4.10 shows the baseline trajectory in blue and the optimal trajectory in red. Moreover in the two dimensional plot, the switching point are shown. In green is highlighted the change from *Traction* to *Transition 1* phase, it is the same point for both the simulations. The blue dots shows the *Transition 1 - Retraction* switch that is in both cases happening at an elevation of $\theta = 1$ but the φ values change. The *Retraction - Transition 2* change is in black while the *Transition 2 - Traction* one is in red.
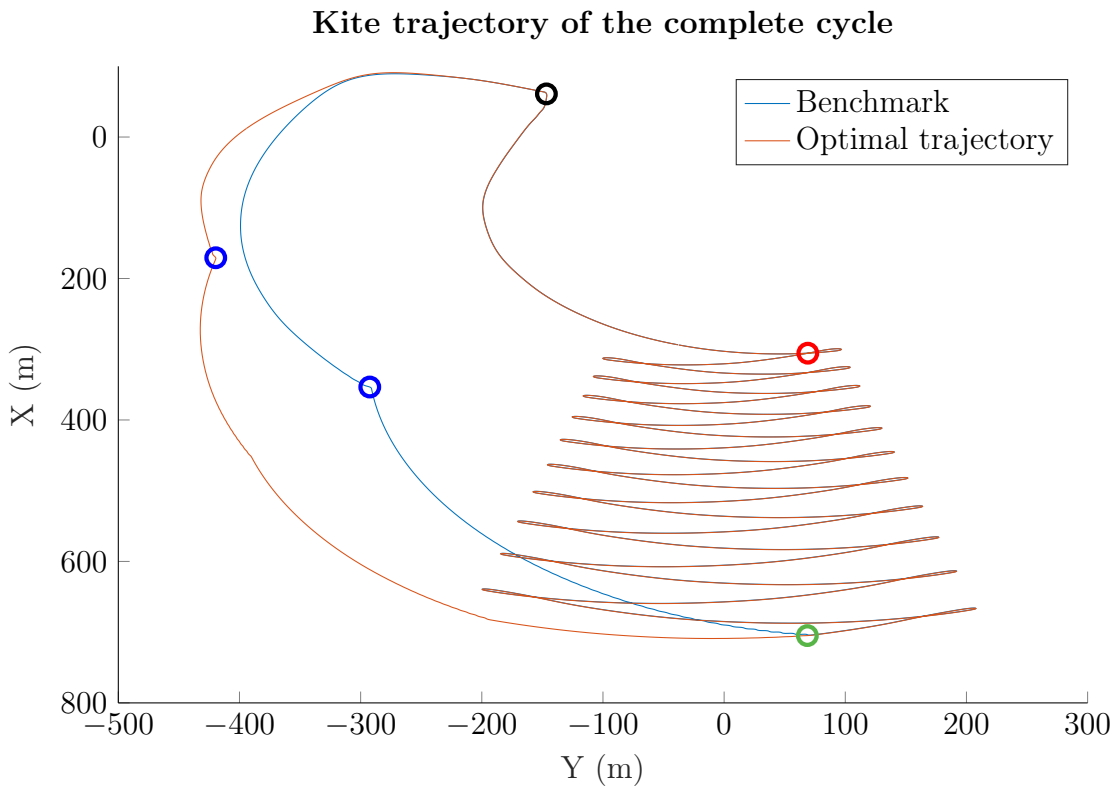
Figure 4.10: The kite's trajectory in the $Y - X$ plane, the dots highlights the change from one phase to the next one. In order: green, blue, black and red.

To quantify the improvement achieved by following the optimal trajectory, the average cycle power of the two solutions shall be compared. With the baseline approach the rated power values was of $114.9[kW]$ while the one obtain by following the red line is equal to $119.1[kW]$. An increased of approximately of 3.7%.

4.2.2. Different nominal wind speed

Once the optimal trajectory at a given wind speed was found, the question arose as to how it varied with varying wind conditions. Hence, the optimization routine was performed several times by varying the wind intensity from 12 m/s down to 6 m/s.

The results obtained are are displayed in the table 4.3 and graphic visualization of the change in the trajectory followed by the kite during *Transition 1* is shown in figure 4.11 and 4.12.

Sim Name		Force estimate strategy						
w0		6	7	8	9	10	11	12
TPs	θ	0.488	0.4312	0.3259	0.3013	0.3597	0.3053	0.3156
		0.6152	0.4967	0.3304	0.3147	0.4598	0.463	0.4761
		0.8122	0.9249	0.4142	0.941	0.6939	0.9074	0.7821
		1.0066	1.0514	1.1069	1.011	1.1471	1.0406	1.0823
	φ	0.5983	0.9583	0.6816	1.4047	0.4359	1.074	0.1848
		0.8691	1.0645	1.3445	1.4047	0.5967	1.074	0.7933
		1.1391	1.2891	1.5433	1.4465	0.7115	1.1867	0.8531
		1.4924	1.5379	1.5697	1.5708	1.4687	1.5371	1.5708
v_trac		1.5086	1.5168	1.5299	1.8448	2.0642	2.4505	2.699
v_retr		-2.9984	-3.6045	-2.8904	-3.3907	-3.7172	-4.3991	-4.7109

Table 4.3: Optimal target points at for the $W \in [6, 12]$ $[m/s]$
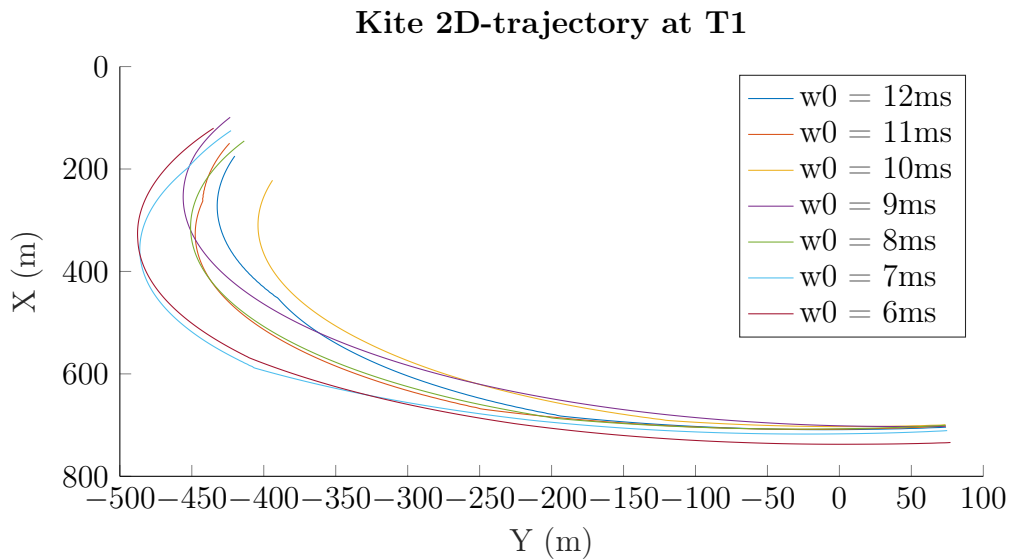
Figure 4.11: Optimal *Transition 1* trajectory at varying wind speed, Y-X plane.

Kite 3D-trajectory at T1
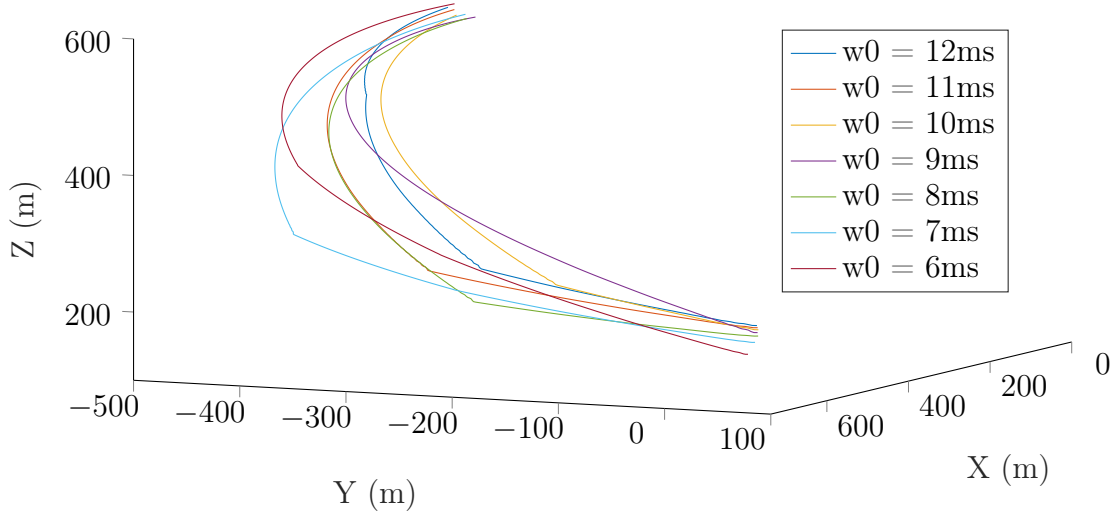
Figure 4.12: Optimal *Transition 1* trajectory at varying wind speed.

The images highlights that the trajectory followed by the kite are all similar for in the entire wind range, that lead to the idea of finding one unique sequence of target points that could be use independently from the wind speed. The term "sub-optimal solution" will be used to refer to such solution.

Each one of the four target point was computed by averaging the values of the optimal θ and φ obtained by varing the wind conditions. The values are reported in the following table, and can be visualised in figure 4.13 and 4.14.

	θ	φ
1	0.3608	0.7625
2	0.4508	1.0210
3	0.7822	1.1670
4	1.0621	1.5353

Table 4.4: Average of the optimal target points at for $W \in [6, 12]\ [m/s]$

Finally to compare the results obtained with the unique sequence of target point with respect to one achieved by following the optimal trajectory, the average cycle power of the two solutions shall be compared. The results are displayed in the table below.

Wind speed W in [m/s]	6	7	8	9	10	11	12
Benchmark [kW]	11.71	20.07	34.30	48.50	66.93	87.81	114.88
Optimal rated power [kW]	13.46	21.78	35.12	49.68	68.65	91.26	119.09
% increase	14.9%	8.5%	2.4%	2.4%	2.6%	3.9%	3.7%
Sub-optimal rated power [kW]	13.46	21.67	35.01	49.66	68.59	90.98	118.79
% increase	14.9%	8.0%	2.1%	2.3%	2.5%	3.6%	3.4%

Table 4.5: Average cycle power production comparison between benchmark, optimal solution, sub-optimal solution.

The results reported in the table 4.5 show that with respect to the benchmark both the approaches provide a significant improvement of the system performances in terms of average cycle power. The sub-optimal solution results don't show a significant deterioration of the performances. This result suggest that one unique trajectory could be used for the *Transition one* regardless form the wind conditions.
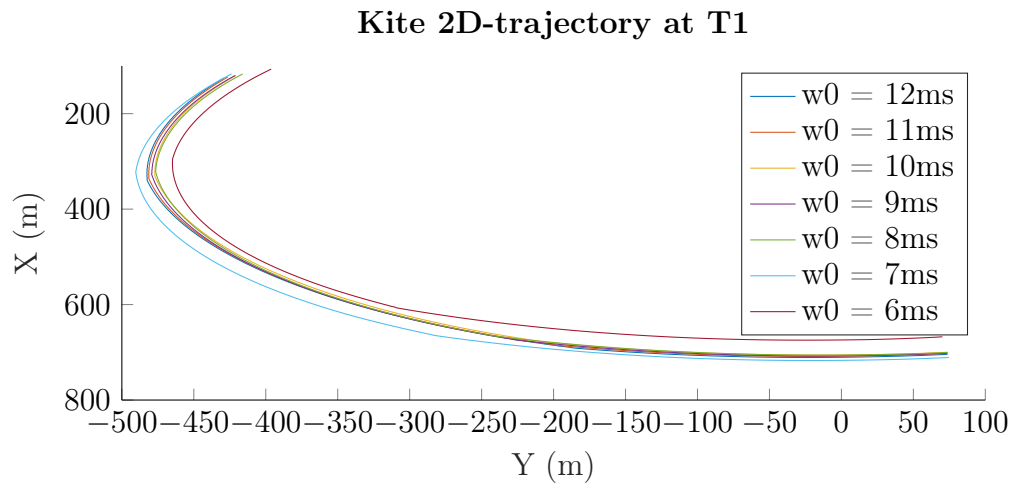
Figure 4.13: Sub-optimal *Transition 1* trajectory at varying wind speed.

Kite 3D-trajectory at T1
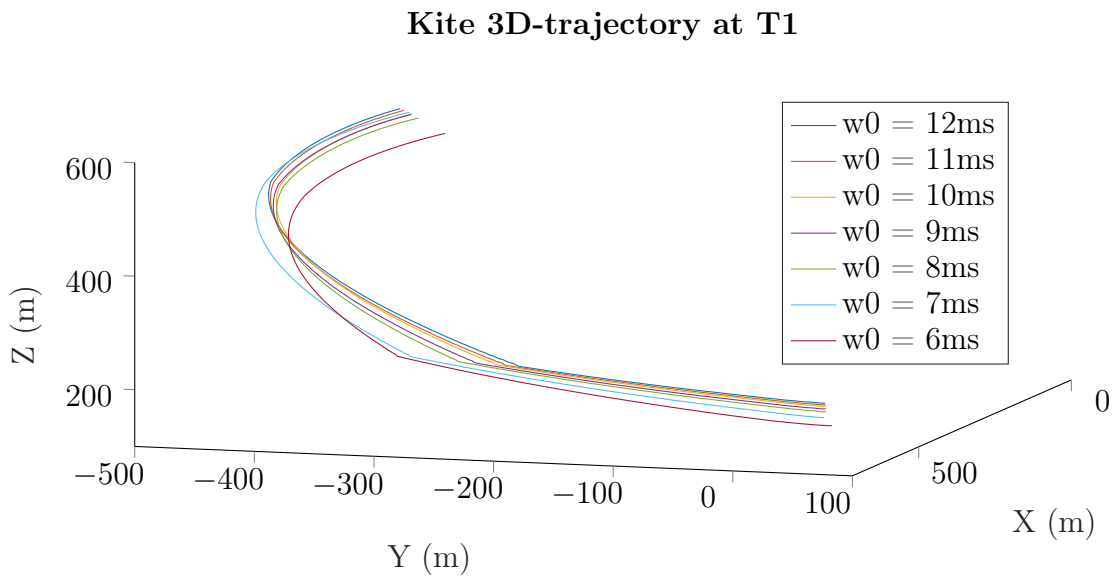
Figure 4.14: Sub-optimal *Transition 1* trajectory at varying wind speed, Y-X plane.

5 | Conclusions and future developments

The goal of this thesis work was to develop a control logic for the phase of pumping airborne wind energy systems that avoids abrupt increase in the force acting on the tether. This solution was implemented in two different ways, the first one exploits the measure of the nominal wind and ensures that the winch controller to follows the desired reeling speed profile. The second implementation is independent of wind measurements and this is desirable feature since such a measurement is often unreliable and not suitable for real world applications. The second goal of this work was to obtain optimal $\theta - \varphi$ trajectory for the *Transition 1* at varying wind speed. The optimality criterion used to evaluates the different solution is the average cycle power. The decoupled structure of the control system was exploited to find the optimal target points to be followed by the kite in order to describe the desired path. This goals have been achieved, providing new results compared to the state of the art, where the transition phase were not well explored The thesis work also opens several directions for further developments. One aspect that could be further tested with more complex and more realistic wind profiles is the logic of the winch controller. If the results obtained in this work were also corroborated by these more complex simulations, it would then be interesting to implement this approach on a real prototype.

Another possible development of this work would consist in the analysis of the optimal trajectory for different initial conditions along the eight figure path, or alternatively the problem could be analyzed with a nested optimization routine, where the outer loop optimize the switching conditions criteria and then an inner optimization problem would compute the associated optimal trajectory. However this second problem could be hard to implement due to the even higher non-linearity of the switching conditions that affects directly the stability of the overall system. A third and final development for this work could be the extension of the obtained results to the *Transition 2*. A similar control structure for the winch could be designed and optimal trajectory could be computed for different wind speed.

Bibliography

[1] The Med gets first offshore wind farm as Italy vows energy revolution. URL `https://www.france24.com/en/live-news/20220316`.

[2] Nozioni fondamentali - La finestra di volo. URL `https://www.kitesalento.it/news/25-nozioni-fondamentali-la-finestra-di-volo`.

[3] Technical catalog: High voltage engineered induction motors. URL `https://search.abb.com/library/Download.aspx?DocumentID=9AKK103508&LanguageCode=en&DocumentPartId=&Action=Launch`.

[4] Onshore Wind Power has a New Face | SkySails Power. URL `https://skysails-power.com/onshore-units/`.

[5] Ultra High Molecular Weight Polyethylene Fiber from DSM Dyneema.

[6] The Sustainable Development Goals Report. 2021. URL `https://unstats.un.org/sdgs/report/2021/The-Sustainable-Development-Goals-Report-2021.pdf`.

[7] ABB. Quaderni di applicazione tecnica N.13 Impianti eolici.

[8] B. Amirzadeh, A. Louhghalam, M. Raessi, and M. Tootkaboni. A computational framework for the analysis of rain-induced erosion in wind turbine blades, part I: Stochastic rain texture model and drop impact simulations. *Journal of Wind Engineering and Industrial Aerodynamics*, 163:33–43, 4 2017. ISSN 0167-6105. doi: 10.1016/J.JWEIA.2016.12.006.

[9] A. Berra and L. Fagiano. An optimal reeling control strategy for pumping airborne wind energy systems without wind speed feedback. Technical report.

[10] M. Bolognini and L. Fagiano. Lidar-based navigation of tethered drone formations in an unknown environment. *IFAC-PapersOnLine*, 53:9426–9431, 2020. ISSN 24058963. doi: 10.1016/J.IFACOL.2020.12.2413.

[11] R. Bosman, V. Reid, M. Vlasblom, and P. Smeets. Airborne Wind Energy Tethers with High-Modulus Polyethylene Fibers. *Green Energy and Technology*, pages 563–

585, 2013. ISSN 18653537. doi: 10.1007/978-3-642-39965-7{_}33. URL `https://link.springer.com/chapter/10.1007/978-3-642-39965-7_33`.

[12] M. Canale, L. Fagiano, and M. Milanese. High altitude wind energy generation using controlled power kites. *IEEE Transactions on Control Systems Technology*, 18(2): 279–293, 3 2010. ISSN 10636536. doi: 10.1109/TCST.2009.2017933.

[13] A. Cherubini, A. Papini, R. Vertechy, and M. Fontana. Airborne Wind Energy Systems: A review of the technologies. *Renewable and Sustainable Energy Reviews*, 51:1461–1476, 8 2015. ISSN 18790690. doi: 10.1016/J.RSER.2015.07.053. URL `http://creativecommons.org/licenses/by/4.0/`.

[14] B. Demirel. *Architectures and performance analysis of wireless control systems*. PhD thesis, 2015.

[15] P. Di Milano. Optimal control of pumping airborne wind energy systems without wind speed feedback. Technical report.

[16] S. Dunker. Tether and Bridle Line Drag in Airborne Wind Energy Applications. *Green Energy and Technology*, 0(9789811019463):29–56, 2018. ISSN 18653537. doi: 10.1007/978-981-10-1947-0{_}2. URL `https://link.springer.com/chapter/10.1007/978-981-10-1947-0_2`.

[17] i. Egypt Yoshida, M. A. Rushdi, S. Yoshida, and T. N. Dief. Simulation of a Tether of a Kite Power System Using a Lumped Mass Model. 4:2018–2028. doi: 10.15017/1960663. URL `https://doi.org/10.15017/1960663`.

[18] I. Energy Agency. World Energy Outlook 2021. 2021. URL `www.iea.org/weo`.

[19] M. Erhard and H. Strauch. Control of towing kites for seagoing vessels. *IEEE Transactions on Control Systems Technology*, 21(5):1629–1640, 9 2013. ISSN 10636536. doi: 10.1109/TCST.2012.2221093.

[20] L. Fagiano and S. Schnez. On the take-off of airborne wind energy systems based on rigid wings. *Renewable Energy*, 107:473–488, 7 2017. ISSN 0960-1481. doi: 10.1016/J.RENENE.2017.02.023.

[21] L. Fagiano, K. Huynh, B. Bamieh, and M. Khammash. On sensor fusion for airborne wind energy systems. *IEEE Transactions on Control Systems Technology*, 22(3): 930–943, 2014. ISSN 10636536. doi: 10.1109/TCST.2013.2269865.

[22] L. Fagiano, A. U. Zgraggen, M. Morari, and M. Khammash. Automatic crosswind flight of tethered wings for airborne wind energy: Modeling, control design, and

experimental results. *IEEE Transactions on Control Systems Technology*, 22(4):1433–1447, 2014. ISSN 10636536. doi: 10.1109/TCST.2013.2279592.

[23] L. Fagiano, M. Quack, F. Bauer, L. Carnel, and E. Oland. Autonomous Airborne Wind Energy systems: accomplishments and challenges. *Annual Review of Control, Robotics, and Autonomous Systems*, 2022. doi: https://doi.org/10.1146/annurev-control-042820-124658. URL `www.annualreviews.org`.

[24] Fagiano Lorenzo Mario. *Control of Tethered Airfoils for High-Altitude Wind Energy Generation*. PhD thesis, Politecnico di Torino, 2009.

[25] U. Fechner, R. van der Vlugt, E. Schreuder, and R. Schmehl. Dynamic model of a pumping kite power system. *Renewable Energy*, 83:705–716, 11 2015. ISSN 0960-1481. doi: 10.1016/J.RENENE.2015.04.028.

[26] M. L. Loyd. Crosswind Kite Power. Technical report, Lawrence Livermore National Laboratory,, Livermore,California, 1980.

[27] Matteo Ciucci. ENERGY POLICY: GENERAL PRINCIPLES. 2021.

[28] R. Read. Kite Networks for HarvestingWind Energy. *Green Energy and Technology*, 0 (9789811019463):515–537, 2018. ISSN 18653537. doi: 10.1007/978-981-10-1947-0{_}21. URL `https://link.springer.com/chapter/10.1007/978-981-10-1947-0_21`.

[29] C. Vermillion, M. Cobb, L. Fagiano, R. Leuthold, M. Diehl, R. S. Smith, T. A. Wood, S. Rapp, R. Schmehl, D. Olinger, and M. Demetriou. Electricity in the air: Insights from two decades of advanced control research and experimental flight testing of airborne wind energy systems. 2021. doi: 10.1016/j.arcontrol.2021.03.002. URL `https://doi.org/10.1016/j.arcontrol.2021.03.002`.

[30] J. Weber, M. Marquis, A. Cooperman, C. Draxl, R. Hammond, J. Jonkman, A. Lemke, A. Lopez, R. Mudafort, M. Optis, O. Roberts, and M. Shields. Airborne Wind Energy. 2021. URL `https://www.nrel.gov/docs/fy21osti/79992.pdf`.

[31] P. Williams, B. Lansdorp, and W. Ockels. Modeling and control of a kite on a variable length flexible inelastic tether. *Collection of Technical Papers - 2007 AIAA Modeling and Simulation Technologies Conference*, 2:852–871, 2007. doi: 10.2514/6.2007-6705. URL `https://arc.aiaa.org/doi/pdf/10.2514/6.2007-6705`.

[32] A. U. Zgraggen, L. Fagiano, and M. Morari. Automatic Retraction and Full-Cycle Operation for a Class of Airborne Wind Energy Generators. *IEEE Transactions on*

Control Systems Technology, 24(2):594–608, 3 2016. ISSN 10636536. doi: 10.1109/TCST.2015.2452230.

A | Simulink models

In this chapter the Matlab/Simulink model developed are displayed.
The simulink model of the kite is reported in the figure below:
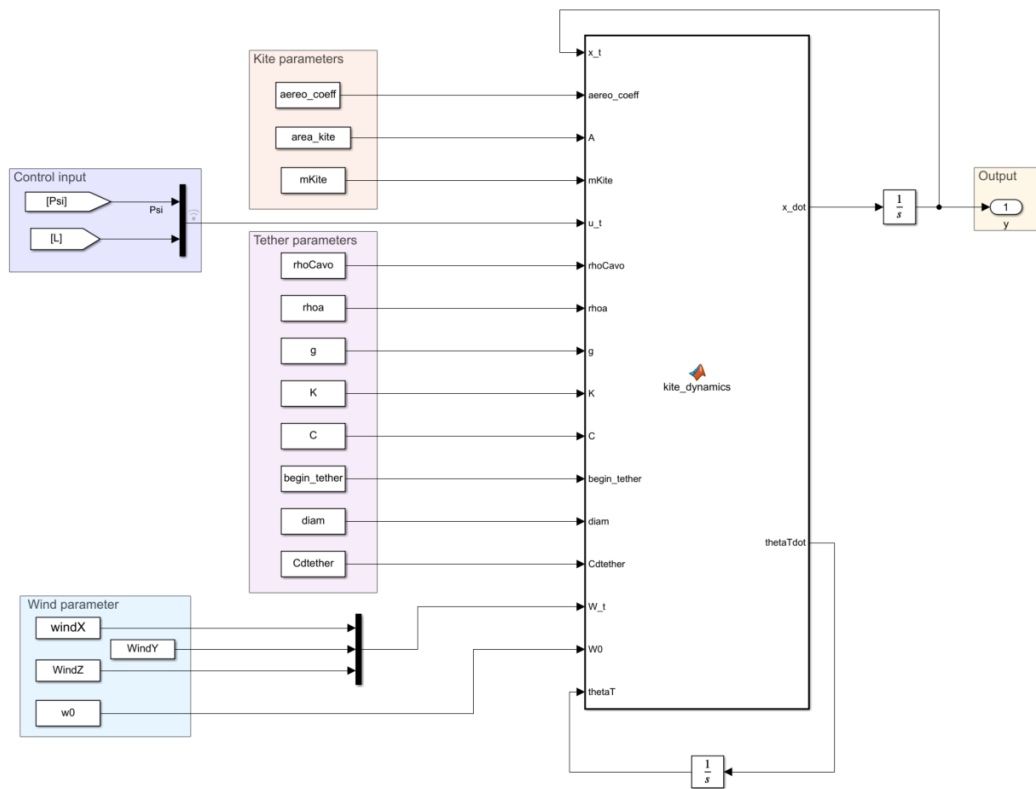
Figure A.1: Simulink scheme of the kite's model

List of Figures

List of Tables

List of Acronyms

Acronyms	Description
AWE	Airborne Wind Energy
BFGS	Broyden–Fletcher–Goldfarb–Shanno algorithm
EU	European Union
GS	Ground Station
GU	Ground Unit
KSU	Kite Steering Unit
STEPS	Stated Policies Scenario
SU	Steering Unit
T1	Transition 1 phase
TES	Total energy supply
TP	Target Point
TPES	Total primary energy supply
UN	United Nations
UV	Ultraviolet radiations

Acknowledgements

A special thanks goes to my thesis advisor Professor Fagiano, for the opportunity given me to work on this fascinating topic and for his invaluable guidance and constant support. To my family and friends for always being there for me.